Impact of Cloud Phase Composition on the Climate Response to Obliquity Forcing

Lily Hahn

Advisors: Trude Storelvmo and Navjit Sagoo

Second Reader: Ron Smith

May 5, 2017

A Senior Thesis presented to the faculty of the Department of Geology and Geophysics, Yale University, in partial fulfillment of the Bachelor's Degree.

Abstract

Earth's orbital cycles of eccentricity, obliquity, and precession have driven past variations in climate, with the global ice-volume record influenced most strongly by obliquity forcing in the early Pleistocene. While proxy records suggest that orbital cycles are responsible for glacial-interglacial cycles, modeling studies have found that cloud feedbacks impede ice sheet initiation by opposing glaciation at times when orbital forcing supports it.   However, a recent study with cloud phase constrained by satellite observations provides evidence for a weaker opposing cloud feedback than previously found in response to carbon dioxide doubling, suggesting that this cloud phase adjustment may also alter the modeled climate response to orbital forcing. Using the same adjusted cloud phase partitioning scheme in comparison with an out-of-the-box (OOTB) setup, radiative feedbacks in response to reduced obliquity are investigated in the Community Earth System Model (CESM), version 1.0.6. With no global annual-mean insolation change, mean temperature changes of -0.8 K in the OOTB model and -1.2 K in the adjusted cloud phase model (SLF) indicate the importance of feedbacks for the climate response. Climate feedbacks also contribute to the extension of negative temperature changes to latitudes with positive insolation changes in both experiments, with temperature reductions encompassing lower latitudes for SLF than OOTB. The water vapor and shortwave cloud feedbacks contribute most to enhanced cooling in the SLF model, as thermodynamic changes strengthen cooling by the water vapor feedback and as increased cloud water content in the mid-latitudes as well as north of 75°N augments reflection of shortwave radiation. With greater cooling extending to lower latitudes in the adjusted cloud phase composition model, our results provide stronger support than previous studies for the obliquity-induced Northern Hemisphere ice sheet growth shown in the paleoclimate record.

1. Introduction

As demonstrated by paleoclimate records and modeling, orbital forcing arising from changes in obliquity, precession, and eccentricity has contributed to Earth's climate variability by altering the distribution of incoming solar radiation (Fig. 1; Hodell 2016). In support of the Milankovitch (1941) theory that orbital cycles drive glacial-interglacial cycles, Hays, Imbrie and Shackleton (1976) found that the Quaternary global ice-volume record varies at orbital frequencies, but stopped short of proposing mechanisms for ice sheet growth and decline. Further studies have found what has been termed the 41-kyr paradox: while high-latitude summer insolation is driven most strongly by the earth's precession, global ice-volume record variability in the early Pleistocene is dominated not by the 23-kyr precession period but by the 41-kyr period of obliquity, or axial tilt (Cortijo et al. 1999; Vimeaux et al. 2001; Raymo and Nisancioglu 2003; Lisiecki and Raymo 2005). With obliquity-driven insolation changes too small to drive the observed glacial-interglacial cycles alone, internal climate processes in response to obliquity changes have been invoked to explain the paleoclimate ice record (e.g., Raymo and Nisancioglu 2003; Lee and Poulsen 2005, 2008). However, as climate models do not simulate large enough climate feedbacks in response to obliquity forcing to match the proxy records, the mechanisms by which obliquity changes contribute to glacial-interglacial cycles are still not understood (Hodell 2016; Maslin 2016).

Mantsis et al. (2011) and Erb et al. (2013) constitute the first climate modeling studies to isolate obliquity changes and to quantitatively assess the climate feedbacks amplifying or dampening obliquity forcing. Both use idealized simulations representing obliquity maximum and minimum values from the past 600 kyr in the GFDL Climate Model, version 2.1 (CM2.1), examining the resulting climate feedbacks, and Erb et al. also investigate the potential for ice sheet initiation in response to reduced obliquity. Reduced obliquity is expected to contribute to Northern Hemisphere ice sheet growth by decreasing insolation and temperature at high latitudes and by increasing the meridional insolation gradient and moisture transport (Lee and Poulsen 2008), enhancing snowfall accumulation and reducing summer melt, with glaciation amplified by the ice-albedo feedback as well as the other fast radiative feedbacks. However, Erb et al. find that their modeled climate feedbacks are too small to drive these changes in glaciation, with modeled cloud feedbacks due to reductions in cloud water content and low-cloud fraction opposing glaciation in response to reduced obliquity.
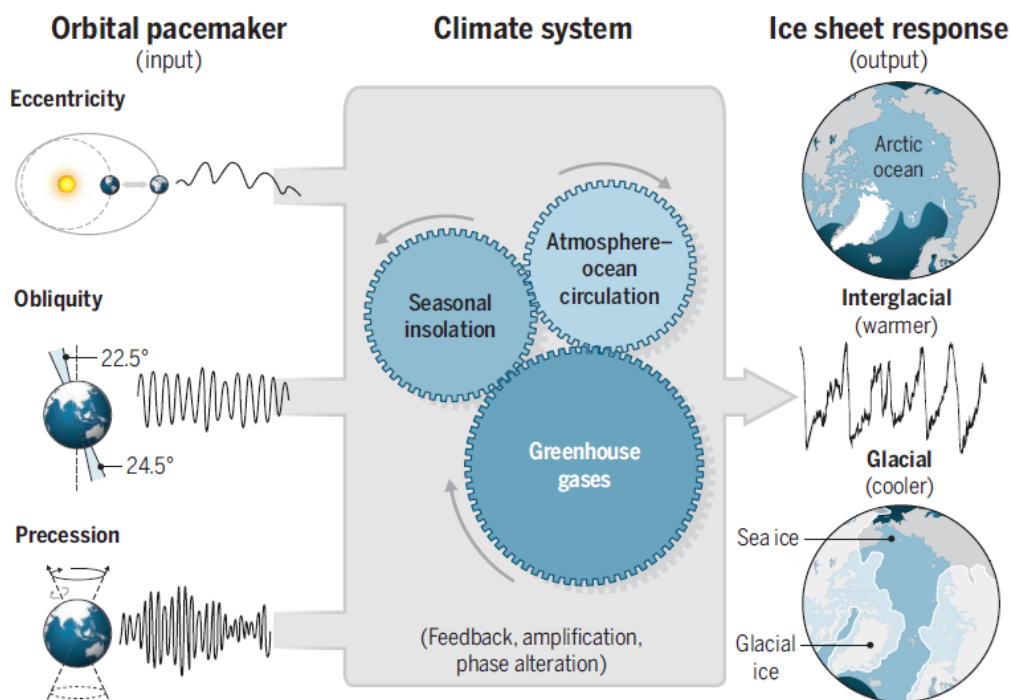
Figure 1. Cyclic variations in Earth's orbital parameters result in climate changes that drive glacial–interglacial cycles (from Hodell 2016).

Our reassessment of the climate response to reduced obliquity is motivated by recent evidence that the cloud phase feedback, which acts to oppose an initial radiative forcing, is overestimated in general circulation models (GCMs). In this feedback, an imposed warming signal moves the liquid-to-ice phase transition isotherm to higher altitudes, such that the atmospheric layer between the initial and final isotherm position undergoes a reduction of ice clouds and an enhancement of liquid clouds and supercooled liquid fractions in mixed-phase clouds (Storelvmo et al. 2015). Due to the smaller size and larger population of liquid droplets relative to ice crystals for a given amount of cloud water (Pruppacher and Klett 1978; Murray et al. 2012), clouds with higher liquid content reflect more shortwave (SW) radiation. As a result, an atmospheric temperature increase will be opposed by the cloud phase feedback's enhancement of reflected SW radiation, and a temperature decrease will be opposed by the cloud phase feedback's reduction of reflected SW radiation.

A recent study by Tan et al. (2016) constraining cloud phase composition with satellite observations provides evidence for a weaker cloud phase feedback than previously estimated in response to a CO_2-doubling. While many GCMs underestimate supercooled liquid fractions

4

(SLFs) in comparison with satellite observations (Komurcu et al. 2014; Cesana et al. 2015), Tan et al. represent higher SLFs in mixed-phase clouds by observationally constraining cloud phase. Tan et al. present two main arguments for why GCMs underestimate SLFs: a) the Wegener-Bergeron-Findeisen (WBF) process for ice crystal growth is too strong in GCMs, converting supercooled liquid to ice too efficiently; and b) observational data is lacking for mixed-phase clouds. To address these issues and to bring modeled SLFs closer to satellite observations, Tan et al. vary six cloud microphysical parameters in 256 parameter combinations, and select the two combinations that produce the lowest error in SLFs compared to satellite observations at all isotherms (Tan et al. 2016, Table S1). Both of these simulated parameter combinations result in higher SLFs consistent with satellite observations, but the present study focuses on the CALIOP-SLF1 simulation. One of the main parameters altered is time-scale for ice crystal growth via the WBF process; retarding this time-scale reduces the WBF-efficiency, increasing SLFs. Another change is that the default ice nucleation scheme, in which ice formation is a function only of temperature, is replaced with one in which ice formation is determined both by temperature and by the availability of ice nuclei (IN).

This modified model results in a liquid-to-ice transition isotherm shifted poleward and upward relative to the control. With fewer and thinner clouds at the higher altitudes of the phase transition isotherm in the modified cloud phase scheme, the phase transition response to either a negative or positive forcing is diminished, weakening the cloud phase feedback in response to either a warming or cooling signal. The cloud phase feedback is further weakened in the modified model because higher latitudes receive relatively low incoming solar radiation, such that phase shifts at high latitudes affect the total SW radiation balance to a lesser degree than phase shifts at lower latitudes. As the cloud phase feedback acts to oppose climate perturbations, weakening this feedback amplifies the climate response to an imposed forcing, resulting in a higher climate sensitivity to CO_2-doubling in Tan et al. (2016) than previously estimated.

Because the cloud phase feedback opposes climate perturbations, and because it can mask other cloud feedbacks as well as water vapor, lapse rate, and surface albedo feedbacks, using a more realistic cloud phase scheme with a weaker cloud phase feedback may significantly enhance the modeled role of climate feedbacks in amplifying the earth's response to obliquity forcing. As a result, we would expect to find enhanced potential for obliquity-induced ice sheet initiation in the CALIOP-SLF1 model than found by Erb et al. (2013). This expectation is

supported by the finding that observational constraints on cloud phase composition weaken the cloud phase feedback most notably in the extratropics (Tan et al. 2016), promoting enhanced cooling at the latitudes most important for glacial inception.

To investigate changes in obliquity-driven climate feedbacks resulting from cloud phase modifications, the idealized experiments in Erb et al. (2013) are repeated here using two versions of the GCM CESM: an out-of-the-box model and a model in which supercooled liquid fraction is constrained using satellite data as in CALIOP-SLF1 (Tan et al. 2016). Both models are described along with the experimental design in section 2, and section 3 outlines the temperature response in each experiment. The kernel method employed by Erb et al. and described by Soden et al. (2008) is used to analyze climate feedbacks in section 4, and section 5 assesses each simulation's potential for ice sheet expansion using snow accumulation and ablation diagnostics. Section 6 discusses ongoing work, including simulation retuning and cloud feedback partitioning to distinguish the contributions of optical depth, altitude, and cloud amount following Zelinka et al. (2012). The final section presents the study's conclusions.

2. Model description and experimental design

This study uses the fully coupled Community Earth System Model (CESM), version 1.0.6 (Hurrell et al. 2013), which includes the following component models: version 5.1 of the National Center for Atmospheric Research's Community Atmosphere Model (CAM5.1, Neale et al. 2012); version 4 of the Community Land Model (CLM4.0; Lawrence et al. 2011; Oleson et al. 2010); version 2 of the LANL Parallel Ocean Program (POP2; Smith et al. 2010); and version 4 of the Los Alamos National Laboratory (LANL) Community Ice Code (CICE4.0; Hunke and Lipscomb 2008). Vegetation and ice sheets are fixed. Atmosphere and land components have a horizontal resolution of 1.9° x 2.5°, with 30 layers in the atmosphere, while ocean and ice components have a nominal 1° resolution, with 60 vertical levels in the ocean.

Out-of-the-box (OOTB) CESM simulations are compared to model runs using the CAM5.1 corrected cloud phase CALIOP-SLF1 model developed by Tan et al. (2016), labeled SLF as it constrains SLFs within mixed-phase clouds using satellite observations. Results are further compared to those presented by Erb et al. (2013), who use the Geophysical Fluid Dynamics Laboratory (GFDL) Climate Model, version 2.1 (CM2.1), with interactive atmosphere, ocean, land, and sea ice components (Delworth et al. 2006) and with fixed

vegetation and ice sheets. Of the sixteen GCMs evaluated by Cesana et al. (2015), GFDL-CM3 and NCAR-CAM5 are two of the thirteen models that underestimate the liquid fraction in mixed-phase clouds at low temperatures corresponding to mid-level and high-level clouds (and low clouds at high latitudes). As GFDL-CM3 and GFDL-CM2.1 use the same scheme described by Rotstayn et al. (2000) to calculate the liquid fraction in mixed-phase clouds (Delworth et al. 2006; GFDL Global Atmospheric Model Development Team 2004; Donner et al. 2011), CM2.1 is also expected to underestimate the mixed-phase cloud liquid fraction. Therefore, we expect both GFDL-CM2.1 and OOTB CESM runs to underestimate SLFs and overestimate the cloud phase feedback in comparison to the weakened cloud phase feedback of the SLF CESM runs, which represent SLFs more realistically.

The equilibrium global mean surface temperature change in response to a doubling of carbon dioxide, or the equilibrium climate sensitivity (ECS), is 3.4°C for CM2.1 (Delworth et al. 2006), 4.0°C for OOTB CESM, and 5.0°C for SLF CESM (Tan et al. 2016), indicating that imposed CO_2 forcing is amplified by climate processes to a greater extent in OOTB CESM than in CM2.1, with the large amplification in SLF CESM attributed by Tan et al. to the model's weakened negative cloud phase feedback. While obliquity forcing differs from CO_2 forcing in magnitude and in latitudinal and seasonal distribution, producing differences in the resulting climate feedbacks (Erb et al. 2013), these ECS values suggest that the climate response may be enhanced in the SLF obliquity runs relative to OOTB obliquity simulations.

In both the OOTB CESM model and modified cloud phase SLF CESM model, two idealized simulations are performed to model extremes in obliquity forcing, using an experimental set-up identical to that of Erb et al. (2013) with the exception of the longitude of perihelion, the default value of which differs slightly between the CESM and GFDL models (Table 1). Obliquity is set to 22.079° in the low obliquity simulation and 24.480° in the high obliquity simulation, replicating the minimum and maximum obliquities of the last 600 kyr of the Quaternary Period (Berger and Loutre 1991). All other variables, including greenhouse gas concentrations and ice sheet extent, are prescribed at preindustrial (1850) levels. In addition to these extreme obliquity simulations, preindustrial control runs are conducted for both the OOTB and SLF CESM models. GFDL-CM2.1 and CCSM3, a predecessor of CESM, are among the better performing models from the Coupled Modeling Intercomparison Project, phase 3 (CMIP3)

7

Table 1. Set-up for obliquity simulations. Simulations below dashed line were conducted by Erb et al. (2013).

Simulation Name	Model	Obliquity (°)	Longitude of Perihelion (°)	Eccentricity
OOTB Lo	OOTB CESM-CAM5.1	22.079	102.7242	0.01671
OOTB Hi	OOTB CESM-CAM5.1	24.480	102.7242	0.01671
OOTB PI	OOTB CESM-CAM5.1	23.441	102.7242	0.01671
SLF Lo	SLF CESM-CAM5.1	22.079	102.7242	0.01671
SLF Hi	SLF CESM-CAM5.1	24.480	102.7242	0.01671
SLF PI	SLF CESM-CAM5.1	23.441	102.7242	0.01671
GFDL Lo	GFDL-CM2.1	22.079	102.932	0.01671
GFDL Hi	GFDL-CM2.1	24.480	102.932	0.01671

in simulations of preindustrial climate, as evaluated by Reichler and Kim (2008, Fig. 1). According to the most recent report by the Intergovernmental Panel on Climate Change (IPCC), CESM-CAM5 and GFDL-CM2.1 also simulate most present-day climatology variables with lower error than the median error of models from the Coupled Modeling Intercomparison Project, phase 5 (CMIP5; Flato et al. 2013, Fig. 9.7).

Simulations were run for 300 years, with the last 50 years used to assess their proximity to an equilibrium state, as indicated by surface temperatures and the top-of-model (TOM) energy balance. The surface temperature time series for these years (Fig. 2) indicates that the OOTB simulations are near equilibrium, with temperature trends of less than 0.04°C/decade. The TOM energy budget for the OOTB Lo, Hi, and PI runs (0.05 W m^{-2}; 0.37 W m^{-2}; and 0.24 W m^{-2}), calculated as the net TOM solar flux minus the net TOM longwave flux, also suggests that the OOTB runs are reasonably balanced. While SLF PI and Hi surface temperatures are close to equilibrium, SLF Lo is less balanced with a trend of -.08 °C/decade, and the SLF runs all show a larger TOM energy imbalance (Lo, -0.83 W m^{-2}; Hi, -0.48 W m^{-2}; PI, -0.57 W m^{-2}) than the OOTB runs, indicating that they are not in equilibrium.

An additional ongoing challenge stems from the temperature difference between the OOTB and SLF runs, as SLF PI is about 3 degrees colder than OOTB PI (Fig. 2). Ideally, SLF PI and OOTB PI would approach similar surface temperatures, such that differences between the SLF and OOTB reduced obliquity experiments could be attributed solely to disparities in the models' treatment of SLFs impacting the climate response to orbital forcing. Instead, because the SLF simulations are colder than the OOTB simulations before obliquity forcing is imposed,
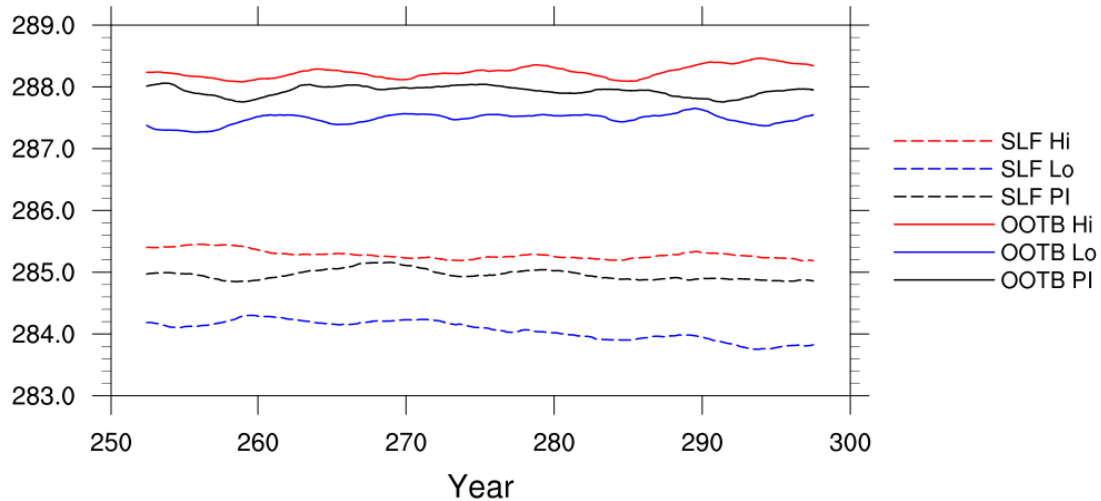
Figure 2. 60-month running mean of global surface temperature time series (K) in the last 50 years of each simulation.

differences between the SLF and OOTB experiments may alternately be due to the higher initial sea ice fraction and resulting surface albedo feedback in SLF. While this temperature difference will be addressed in future simulation re-tuning, which will also aim to bring the SLF runs closer to equilibrium, current results suggest that cloud phase modifications contribute more to an enhanced SLF climate feedback response to reduced obliquity than do differences in initial temperature and sea ice fraction.

Results presented in this study are based on the average climatology over the final 50 years of each simulation. To enable comparison with previous studies modeling obliquity forcing, results are presented in terms of the low obliquity simulation minus the high obliquity simulation (Lo-Hi) for both the OOTB and SLF experiments.

3. Insolation change and temperature response

Previous studies isolating the climate response to reduced obliquity in GFDL CM2.1 (Mantsis et al. 2011; Erb et al. 2013) have found global mean surface air temperature changes (ΔT) of about -0.5°C despite a global annual-mean insolation change of zero. With a top-of-atmosphere (TOA) annual solar insolation increase of several watts per square meter in the tropics and a reduction of up to 16 W/m^2 at high latitudes, these simulations produce surface warming in the tropics and cooling at mid- to high latitudes, with negative temperature changes extending farther equatorward than negative insolation changes. Both studies suggest that this

9

temperature response indicates the importance of radiative feedbacks, which can overpower local radiative forcing.

TOA insolation in the OOTB and SLF Lo-Hi experiments is identical to that of Mantsis et al. (2011) and Erb et al. (2013), with reduced obliquity enhancing the equator-to-pole insolation gradient (Fig. 3a) and reducing extratropical summer insolation in both hemispheres (Fig. 4a). Global mean ΔT is equal to –0.8 K in the OOTB experiment and –1.2 K in the SLF experiment, more than double the GFDL ΔT of –.5 K. The OOTB Lo-Hi annual-mean (Fig. 3b) and seasonal (Fig. 4b) ΔT distribution is similar to that of GFDL Lo-Hi, exhibiting cooling at higher latitudes and warming near the equator, with some cooling at latitudes with positive insolation changes. In contrast, SLF Lo-Hi annual-mean (Fig. 3c) and seasonal (Fig. 4c) ΔT is negative almost everywhere despite the positive insolation changes in the tropics, demonstrating a larger obliquity-induced climate response from SLF.

Erb et al. (2013) and Mantsis et al. (2011) are preceded by several other reduced obliquity simulations which have found surface warming throughout most of the tropics, with cooling limited to higher latitudes (Phillips and Held 1994; Lee and Poulsen 2005). In contrast, the available proxy records based on alkenone productivity and Mg/Ca ratios from foraminifera shells demonstrate tropical cooling from 1° to 2°C in response to reduced obliquity (Mantsis et al. 2011). While the OOTB Lo-Hi experiment demonstrates a surface warming signal throughout the tropics, the extension of surface cooling to the tropics in the SLF Lo-Hi experiment is more consistent with the proxy record than the results of past studies. Mantsis et al. (2011) suggest that the underestimation of tropical cooling in these studies may stem from proxy record uncertainties, the lack of CO_2 variation and dynamic ice sheets in the models employed, or misrepresentation of other dynamical processes or feedbacks which could overwhelm the relatively small imposed radiative forcing in the tropics. Our results support the latter possibility, as the SLF Lo-Hi experiment differs from the OOTB Lo-Hi experiment via model modifications impacting the cloud phase feedback. As discussed in the following section, the SLF experiment's tropical temperature reductions result primarily from the stronger cooling effect of the SW cloud feedback and the amplification of this cooling by the water vapor feedback, although the higher initial sea ice fraction in SLF also contributes to bringing simulated surface temperatures closer to the proxy record.
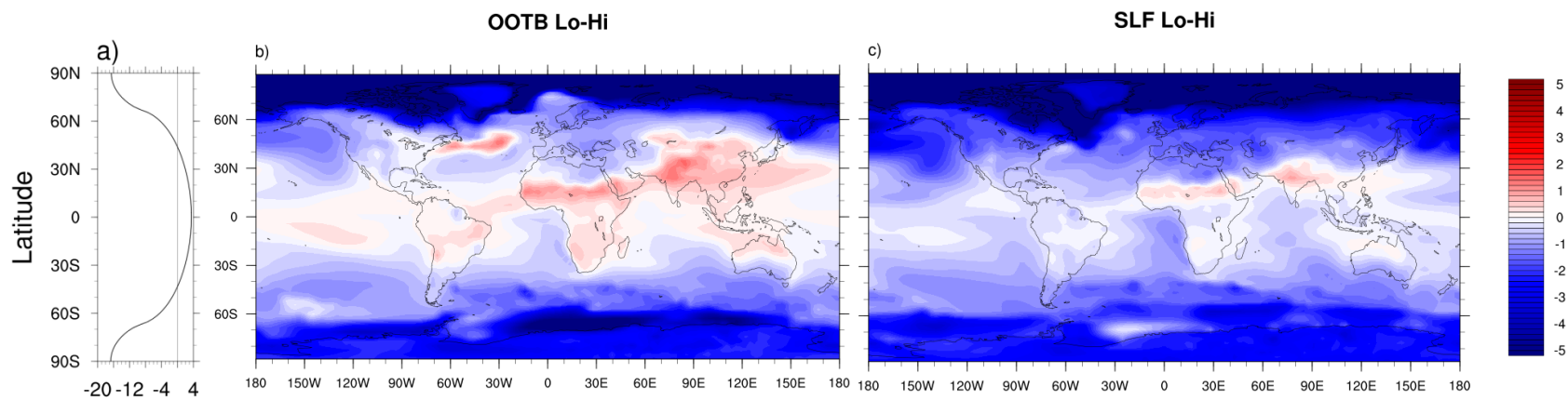
Figure 3. Change in a) OOTB and SLF zonal-mean insolation (W m^{-2}) and in b) OOTB and c) SLF ΔT (K) for the Lo-Hi experiments.
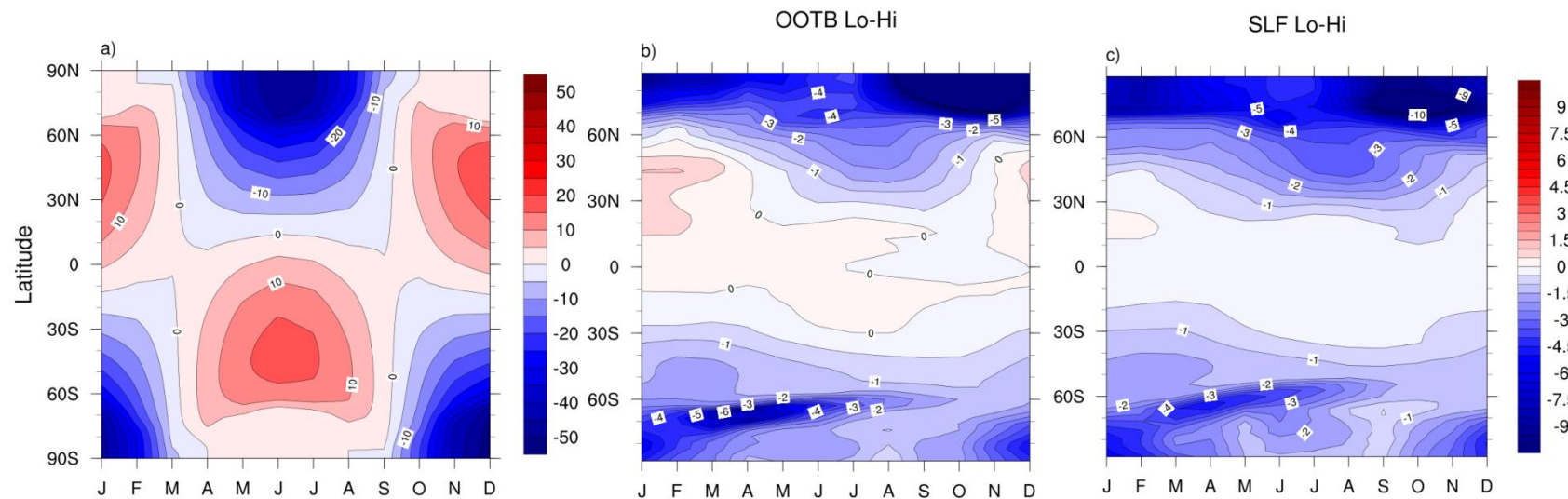

Figure 4. Seasonal changes in a) OOTB and SLF zonal-mean insolation (W m^{-2}) and in b) OOTB and c) SLF ΔT (K) for the Lo-Hi experiments.

4. Radiative feedbacks using the kernel method

This study analyzes the contribution of radiative feedbacks to changes in TOA radiation as in Erb et al. (2013), focusing on surface albedo, atmospheric water vapor, vertical temperature lapse rate, and cloud feedbacks. As these simulations lack active vegetation, the surface albedo feedback arises primarily from changes in snow and ice, which amplify an imposed radiative forcing by enhancing or reducing the reflection of SW radiation. Climate perturbations may also be enhanced by the water vapor feedback, as changes in temperature result in changes in atmospheric water vapor concentration following the Clausius-Clapeyron equation, altering the absorption of longwave (LW) radiation by this greenhouse gas, with smaller effects on SW radiation. Tropospheric changes in the vertical temperature profile, or lapse rate, impact the climate response by altering LW emission, as the majority of outgoing LW radiation originates from the upper troposphere and is thus controlled by upper tropospheric temperatures. Lastly, changes in cloud amount, altitude, and optical depth affect the reflection and absorption of SW radiation as well as the emission and absorption of LW radiation.

As provided by Erb et al. (2013), the following equation gives the total climate sensitivity dF/dT as the sum of the blackbody sensitivity $\delta F/\delta T$ and the fast radiative feedbacks, which can be expressed as the product of a) the change in radiative forcing F per unit change in a given climate variable (surface albedo α_s; atmospheric water vapor q; lapse rate Γ; and cloud optical properties c) and b) the change in this climate variable normalized by the change in surface temperature T:

$$\frac{dF}{dT} = \frac{\delta F}{\delta T} + \frac{\delta F}{\delta \alpha_s}\frac{\delta \alpha_s}{\delta T} + \frac{\delta F}{\delta q}\frac{\delta q}{\delta T} + \frac{\delta F}{\delta \Gamma}\frac{\delta \Gamma}{\delta T} + \frac{\delta F}{\delta c}\frac{\delta c}{\delta T}$$

Each radiative feedback is calculated using the relatively computationally inexpensive kernel method described in Soden et al. (2008). This method separates each feedback into the climate variable change in response to a given temperature change (e.g., dashed box in above albedo feedback expression) and the effect of that climate variable change on the TOA radiative budget, termed the radiative kernel (e.g., solid box in above albedo feedback expression), with the product of these two components giving the feedback. As the kernel method relies on the linearity of climate feedbacks, a slightly different method is used to calculate the cloud feedback, which is nonlinear. The kernel method is used to calculate the effect of noncloud variables (temperature, water vapor, and surface albedo) on the change in cloud radiative forcing (ΔCRF),

which is subtracted from the total ΔCRF to obtain the cloud feedback (Shell et al. 2008). While climate changes in response to reduced obliquity are obtained using the SLF and OOTB Lo-Hi simulations, the radiative kernels employed have been calculated by Shell et al. (2008) using an offline radiative transfer version of the Community Atmospheric Model, version 3 (CAM3). The kernel technique has been shown to underestimate the global clear-sky shortwave feedback by 23% as a result of using monthly-averaged kernels and climate variables (Shell et al. 2008), but a similar bias might be expected from the analysis of Erb et al. (2013), which also employs monthly-averaged kernels.

As in Erb et al. (2013), results are here expressed not as feedbacks (W m^{-2} K^{-1}) but as the impact of feedbacks on the net TOA radiation ΔR$_{net}$ (W m^{-2}) in order to avoid dividing by small global mean ΔT values, and positive values of ΔR$_{net}$ signify increased net downward radiation. The role of the sum of radiative feedbacks as well as each individual feedback is discussed below, with global and regional feedback averages for each CESM experiment provided in Appendix A, along with feedback values given by Erb et al. for the GFDL Lo-Hi experiment.

a) Total feedbacks

The total impact of surface albedo, water vapor, lapse rate, and cloud feedbacks on ΔR$_{net}$ in the Lo-Hi obliquity experiments is shown in Fig. 5i for the OOTB experiment and in Fig. 5j for the SLF experiment. Negative ΔR$_{net}$ values extend to lower latitudes in SLF Lo-Hi than in OOTB Lo-Hi, contributing to the negative temperature response modeled at these latitudes in the SLF experiment. Global annual-mean ΔR$_{net}$ is much larger for SLF (-4.49 W m^{-2}) than for the GFDL (-2.03 W m^{-2}) and OOTB (-2.80 W m^{-2}) simulations, with the SW cloud feedback and the water vapor feedback contributing most strongly to elevated cooling in the SLF experiment compared to the GFDL and OOTB experiments (Table A1). While the lapse rate and cloud feedbacks have the strongest influence on total ΔR$_{net}$ in GFDL and OOTB Lo-Hi, with a relatively small contribution from the water vapor feedback, the water vapor feedback becomes more important in SLF Lo-Hi, second only to the cloud feedback in its impact on the global mean ΔR$_{net}$.

Fig. 6a illustrates the small water vapor feedback effect at all latitudes in the OOTB experiment, while the other feedbacks grow stronger and more negative in the extratropics, with the exception of the positive LW cloud feedback effect. In the SLF experiment, the effect of the
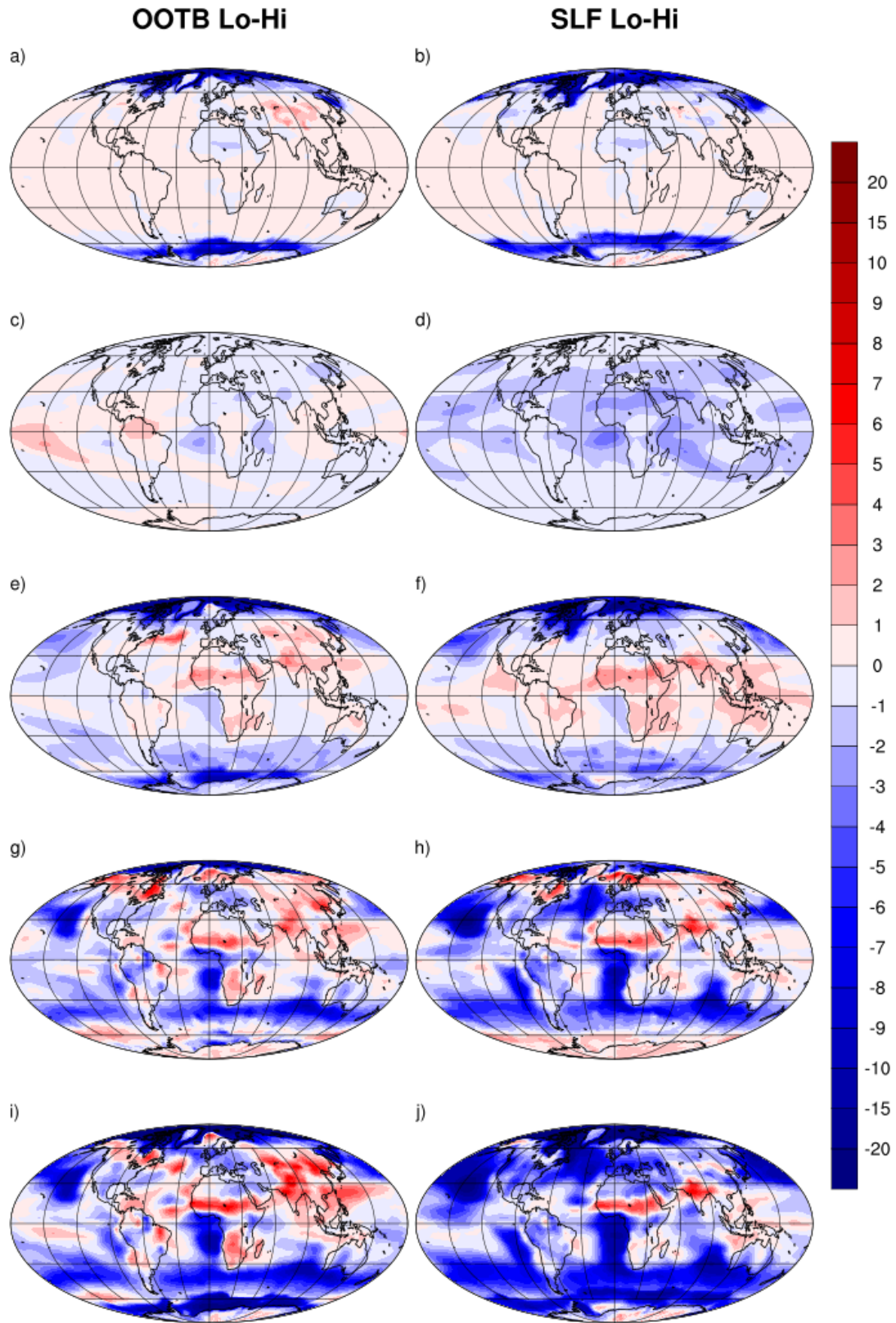
Figure 5. Effect of radiative feedbacks on ΔR_{net} (W m^{-2}), due to a), b) surface albedo; c), d) water vapor; e), f) lapse rate; g), h) clouds; and i), j) total feedbacks for the Lo-Hi OOTB (left) and SLF (right) experiments. Positive values indicate increased net downward radiation.
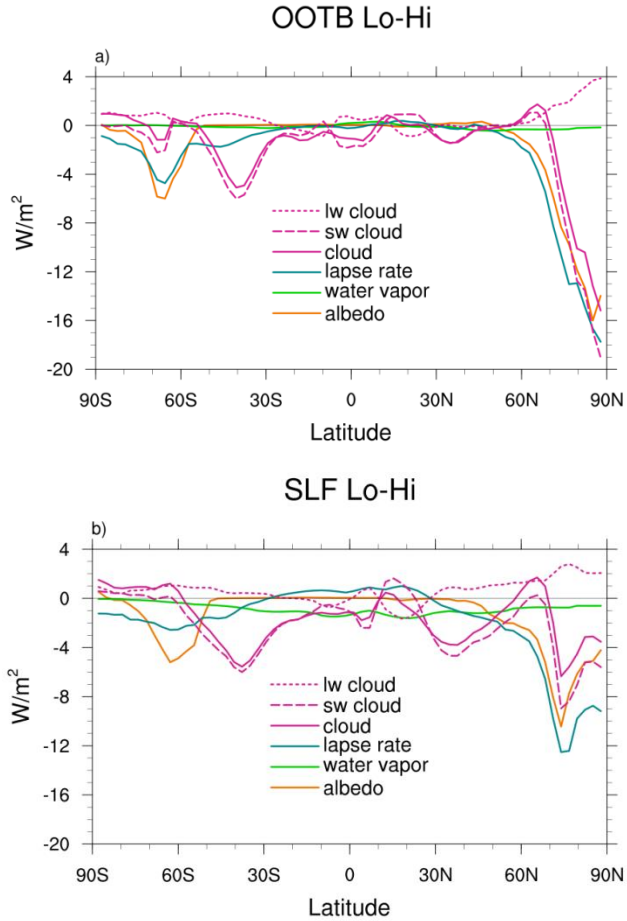
14

OOTB Lo-Hi

SLF Lo-Hi

Figure 6. Effect of feedbacks on zonal-mean ΔR_{net} (W m^{-2}) in a) OOTB Lo-Hi and b) SLF Lo-Hi.

water vapor feedback becomes more negative particularly at lower latitudes (Fig. 6b), with a weakly positive lapse rate feedback at these latitudes. Other key changes in SLF as compared to OOTB include the enhanced SW cloud feedback effect from 30 to 60°N and the weaker cloud, albedo, and lapse rate feedback effects from 75 to 90°N in SLF. We argue that weakened high-latitude feedback changes in SLF Lo-Hi result from the larger initial sea ice fraction and therefore lower sea ice growth potential in this simulation, while strengthened low- and mid-latitude feedback effects in SLF Lo-Hi result primarily from cloud phase treatment differences and secondarily from the colder initial temperatures in SLF. Mechanisms for these differences are discussed in the following sections.

b) Surface albedo feedback

Global mean Lo-Hi ΔR_{net} resulting from the surface albedo feedback is -0.27 W m^{-2} for GFDL,-0.64 W m^{-2} for OOTB, and -0.84 W m^{-2} for SLF, indicating a cooling effect in all three experiments. The ΔR_{net} from this feedback (Figs. 5a and 5b, Fig. 6) results largely from changes in sea ice fraction, as increased sea ice fraction in response to negative insolation changes at high latitudes enhances the reflection of SW radiation, with a net cooling effect. The surface albedo feedback becomes most important poleward of the 60° latitude in both SLF and OOTB as a result of these sea ice changes, with a lower albedo change in the southern hemisphere (SH) than the northern hemisphere (NH) due to the permanent, thermally isolated Antarctic ice sheet. Increased continental snowfall at high latitudes in both OOTB and SLF Lo-Hi also contributes to
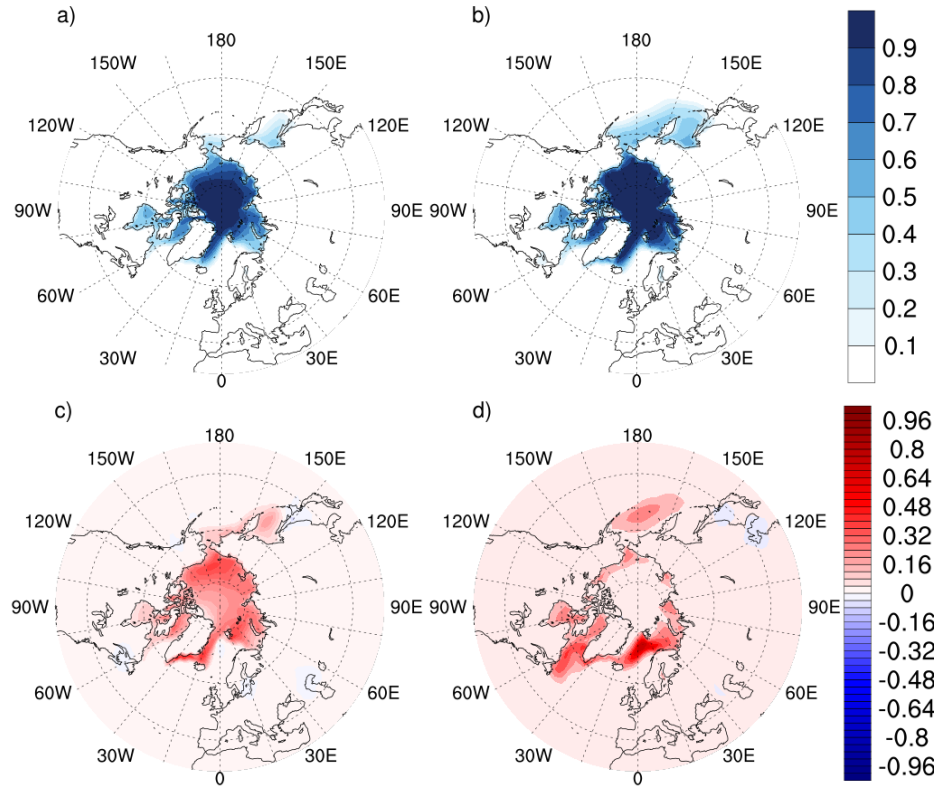
15

Figure 7. Fraction of surface area covered by sea ice above 30 °N in the NH for a) PI OOTB and b) PI SLF, and change in sea ice fraction for c) OOTB Lo-Hi and d) SLF Lo-Hi.

the negative surface albedo effect on ΔR_{net}, and is more important in the NH than the SH due to the larger mid-latitude continental area in the NH.

Differences in the albedo feedback of each experiment arise partly from differences in PI sea ice fractions (Fig. 7a, b). Because the SLF PI simulation is colder than the OOTB PI simulation, and has more sea ice extending to lower latitudes in the Arctic, there is less potential for high latitude sea ice changes in SLF Lo-Hi than in OOTB Lo-Hi (Fig. 7c, d). Weaker sea ice changes at high latitudes in SLF Lo-Hi produce a weaker albedo feedback from about 75 to 90°N compared to the OOTB Lo-Hi feedback, lowering the reflection of SW radiation by this feedback and producing less cooling above 75°N. However, sea ice fraction increases at slightly lower latitudes in SLF Lo-Hi than in OOTB Lo-Hi, enhancing the SLF albedo feedback effect in the Labrador Sea and in the Greenland and Barents Seas. Increased continental snow cover over the southern tip of Baffin Island may also contribute to the enhanced albedo effect at lower latitudes in SLF than in OOTB. While the extension of snow cover and sea ice to lower latitudes in SLF likely results in part from the larger initial sea ice extent in SLF, snow and ice differences

between SLF and OOTB are also promoted by enhanced cooling in SLF Lo-Hi due to the treatment of cloud phase, as discussed in section 1e.

c) Water vapor feedback

The effect of the water vapor feedback (Figure 5c, d, Figure 6) on global mean ΔR_{net} is significantly enhanced in SLF Lo-Hi (-1.02 W m^{-2}) compared to GFDL Lo-Hi (-0.20 W m^{-2}) and OOTB Lo-Hi (-0.09 W m^{-2}). While this feedback contributes slightly positive tropical and negative extratropical effects on the ΔR_{net} in the OOTB and GFDL experiments, its impact on the ΔR_{net} in the SLF experiment is negative at all latitudes, and is particularly strong in the tropics, where water vapor concentrations are the highest.

Water vapor changes may result both from dynamic changes in atmospheric circulation and from thermodynamic changes, in which reduced temperatures produce lower specific humidity values if the relative humidity is constant, following the Clausius-Clapeyron equation. In response to the enhanced meridional circulation gradient in all Lo-Hi experiments, enhancement of the Hadley circulation is expected, which would increase water vapor in the tropics by intensifying the ascension of air at the intertropical convergence zone (ITCZ) and would reduce water vapor in the subtropics by enhancing descending air at these latitudes. The Lo-Hi change in the zonal mean meridional stream function (Fig. 8) demonstrates Hadley circulation intensification in both the OOTB and SLF Lo-Hi experiments, suggesting that dynamical changes may be important for changes in water vapor in both experiments but may not fully account for the water vapor differences between the two experiments.
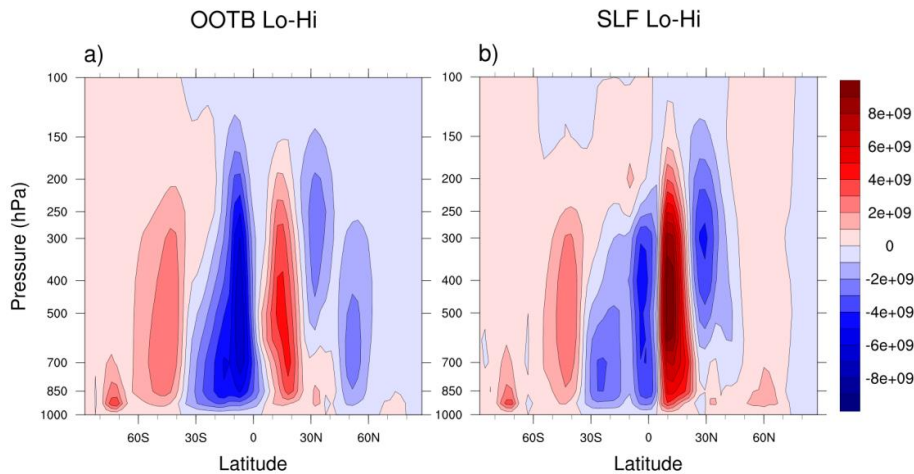

Figure 8. Changes in the zonal-mean meridional stream function (kg/s) calculated for the zonal-mean meridional wind for a) OOTB Lo-Hi and b) SLF Lo-Hi. Positive values indicate enhanced clockwise meridional circulation.

17

The relative contributions of dynamic and thermodynamic changes to the water vapor feedback are further investigated by calculating changes in the thermodynamic and dynamic components of specific humidity in each CESM experiment, following the method used by Erb et al. (2013) and Mantsis et al. (2011). In this method, the thermodynamic part of the change in specific humidity is calculated as the specific humidity change resulting from ΔT at a fixed relative humidity, and subtracting this from the actual change in specific humidity provides an estimation of the dynamic part of the specific humidity change. Erb et al. (2013) find that both the dynamic and thermodynamic components in GFDL Lo-Hi contribute to increased water vapor in the tropics and reduced subtropical water vapor, with thermodynamic changes resulting from reduced temperatures largely accounting for reduced water vapor in the extratropics. While
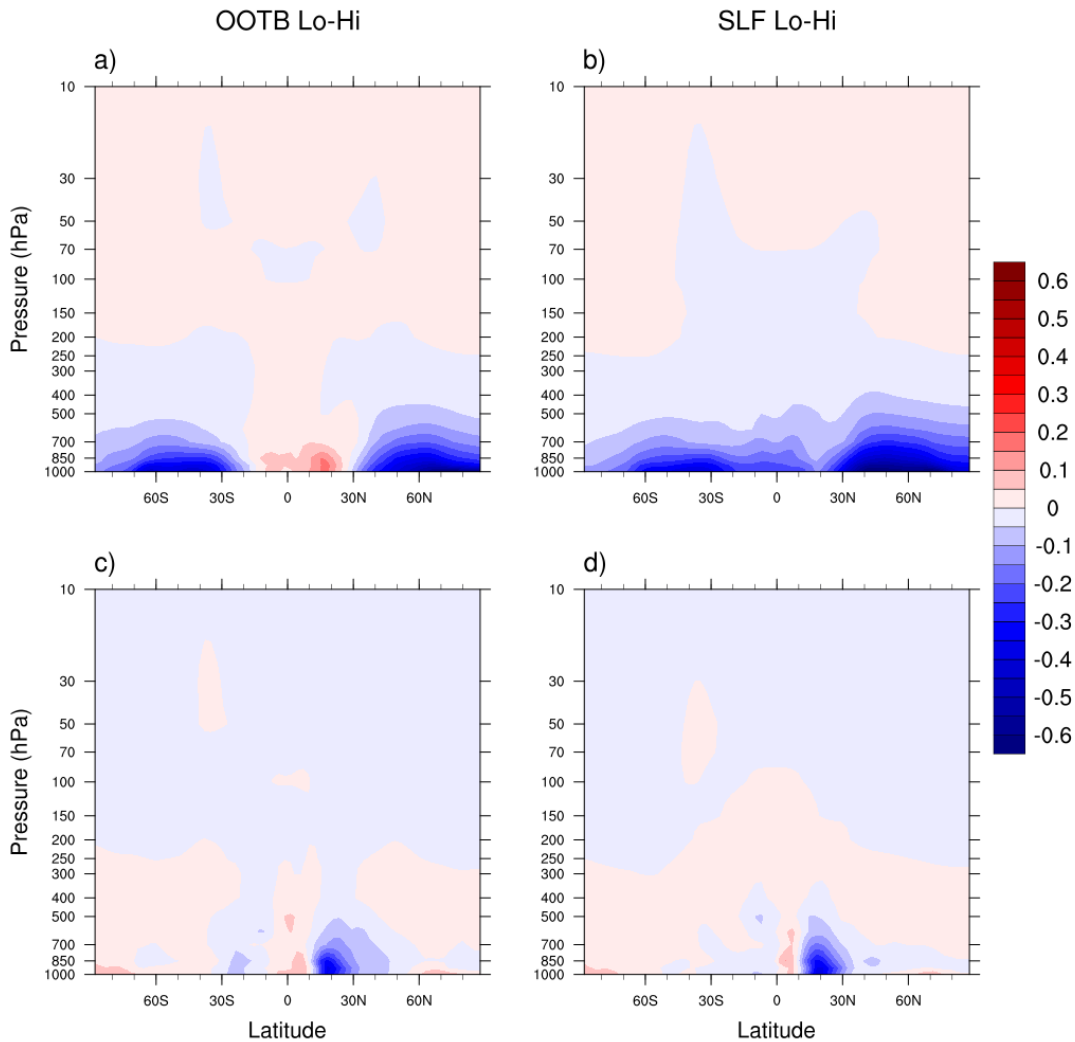

Figure 9. Changes in a), b) thermodynamic component of specific humidity, and c), d) dynamic component of specific humidity (g kg^{-1}) for the (left) OOTB and (right) SLF Lo-Hi experiments.

18

OOTB Lo-Hi also exhibits increased tropical water vapor due to temperature increases and Hadley cell intensification (Fig. 9a, c), with reductions in extratropical water vapor explained largely by temperature reductions at these latitudes, SLF Lo-Hi behaves differently. In SLF Lo-Hi, Hadley cell intensification does contribute to increased water vapor near the ITCZ and reduced water vapor in the subtropics (Fig. 9d), but thermodynamic changes reduce water vapor concentrations at all latitudes and ultimately overwhelm the positive dynamic water vapor changes near the ITCZ (Fig. 9b). In response to nearly global cooling, thermodynamically reduced water vapor dominates the water vapor response at all latitudes in SLF Lo-Hi, reducing the absorption of outgoing LW radiation by this greenhouse gas and further amplifying the global cooling effect. The strength of the water vapor feedback predominantly at low latitudes may be attributed to the initial presence of higher water vapor concentrations in the tropics, allowing for greater reductions at these latitudes than at higher latitudes with lower water vapor concentrations. The remaining question of why the global cooling amplified by the water vapor feedback occurs in the first place, despite positive insolation changes in the tropics resulting from reduced obliquity, will be addressed in the cloud feedback section.

d) Lapse rate feedback

The effect of the lapse rate feedback on ΔR_{net} is shown in Fig. 5e, 5f, and 6, with similar global mean ΔR_{net} values of -0.90 W m^{-2} (GFDL Lo-Hi), -1.03 W m^{-2} (OOTB Lo-Hi), and -0.85 W m^{-2} (SLF Lo-Hi) in the three experiments. The OOTB and SLF latitudinal distributions of lapse rate feedback effects are similar in that the high latitudes are impacted more than low latitudes, with a cooling effect in the extratropics. In response to an imposed forcing, lower latitudes typically undergo larger ΔT aloft than near the surface, while at mid- to high latitudes ΔT is enhanced more at the surface than aloft (Bony et al. 2006). As most of the infrared radiation emitted to space originates from the upper troposphere, a larger ΔT aloft (relative to the surface) in the tropics results in infrared emission changes opposing the initial climate perturbation, while a larger ΔT near the surface at higher latitudes results in infrared emission changes amplifying the initial climate perturbation.

While Erb et al. (2013) find a near zero ΔR_{net} from the lapse rate feedback in the tropics for GFDL Lo-Hi, their negative lapse rate effect on ΔR_{net} at higher latitudes in response to negative insolation changes is consistent with having a larger temperature reduction at the

surface than aloft at these latitudes. Similarly, OOTB and SLF Lo-Hi lapse rate feedbacks produce negative ΔR_{net} values at high latitudes as a result of undergoing stronger cooling at the surface than aloft (Fig. 10). Compared to very small lapse rate feedback effects at low latitudes in OOTB and GFDL, SLF Lo-Hi demonstrates a small, positive lapse rate effect in the tropics, which is consistent with the smaller surface cooling and larger upper troposphere cooling in the tropics (Fig. 10b). Poleward of about 75°N, the stronger negative ΔR_{net} from the lapse rate feedback in OOTB compared to SLF is explained by the vertical gradient in temperature changes in OOTB and SLF, as there is much stronger cooling at the surface than aloft in OOTB while cooling in SLF extends to higher altitudes. The extension of polar cooling to higher altitudes in SLF may partly arise from the greater initial sea ice extent in SLF, but is also related to the weakened cloud phase feedback, as discussed in the following section. The slightly less negative global mean ΔR_{net} from the lapse rate feedback in SLF Lo-Hi compared to OOTB Lo-Hi therefore results mainly from the strengthened positive ΔR_{net} in the tropics in SLF and from the weakened negative ΔR_{net} in the Arctic in SLF.
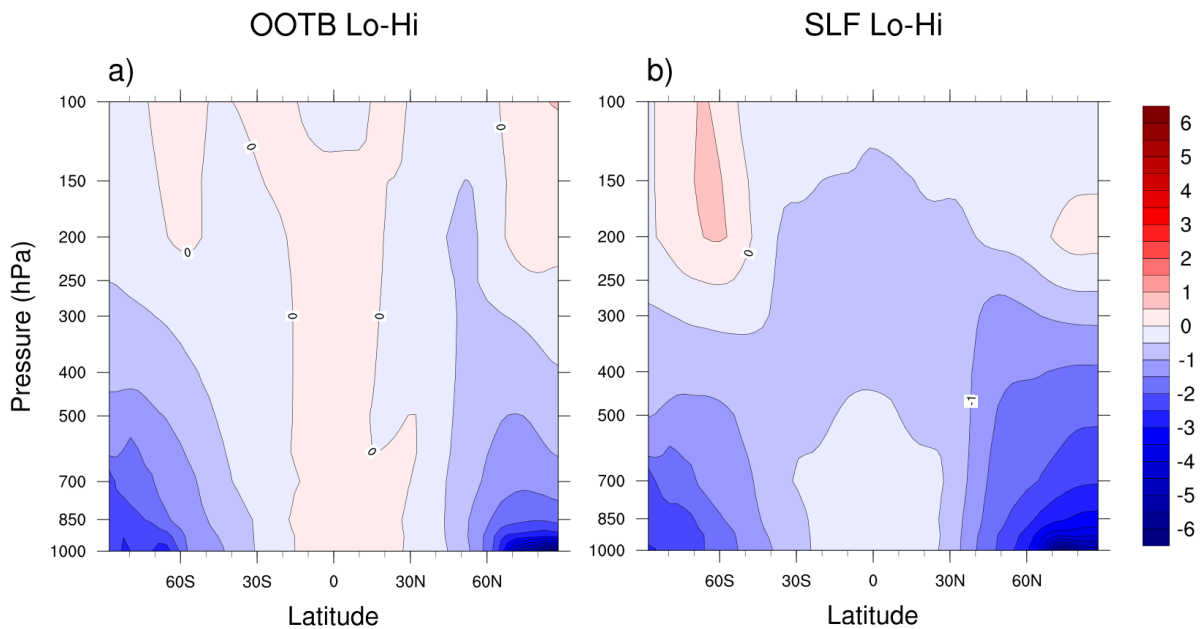

Figure 10. Change in zonal mean temperature (K) in the a) OOTB Lo-Hi and b) SLF Lo-Hi experiments.

e) Cloud Feedback

ΔR_{net} from the cloud feedback is shown in Fig. 5g and 5h for the OOTB and SLF Lo-Hi experiments, with the zonal mean ΔR_{net} shown in Fig. 6. The global mean cloud feedback effect on ΔR_{net} in the Lo-Hi experiments is largest in SLF (-1.77 W m^{-2}), as compared with OOTB (-1.04 W m^{-2}) and GFDL (-0.67 W m^{-2}). As in the GFDL Lo-Hi experiment, clouds in both the OOTB and SLF Lo-Hi experiments have a much larger effect on SW radiation than LW radiation, and the small LW effect of clouds is opposite in sign to the SW effect at most latitudes.

The SW feedback effect is largely explained by changes in cloud liquid and ice water content. Increased cloud liquid and ice content due to reduced temperatures enhances cloud albedo, increasing the reflection of SW radiation. As shown in Fig. 11, regions with increased (reduced) liquid content generally correspond to regions with an enhanced (weakened) negative SW cloud feedback effect, particularly for SLF. Increased ice water content also tends to correlate with an enhanced negative SW cloud ΔR_{net}, with the total ice and liquid water content corresponding best to changes in the SW radiative budget.

The largest change contributing to the stronger negative ΔR_{net} from the SW cloud feedback in SLF compared to OOTB occurs in the mid-latitudes, where stronger increased liquid water path in SLF produces optically thicker clouds and a strengthened, broadened mid-latitude cooling effect in both hemispheres. In the NH mid-latitudes, SLF also shows larger increases in the ice water path than OOTB, further contributing to the reflection of SW radiation with a smaller longwave radiative warming impact. Fig. 12 addresses the question of why the liquid water path in SLF is enhanced in comparison to OOTB, as for any given isotherm the cloud liquid fraction in the observationally constrained SLF model is higher than in the OOTB model. The liquid water fraction was also normalized by the frequency of clouds at a given isotherm, revealing significantly higher normalized liquid water fractions in SLF than in OOTB at all isotherms assessed (-10°C, -15°C, -20°C, -25°C, -30°C, and -35°C). As discussed earlier, because the liquid-to-ice transition isotherm exists at higher altitudes and latitudes in SLF, the positive ΔR_{net} due to the cloud phase feedback is diminished, allowing for a higher liquid water path and more cooling in SLF. The largest SW ΔR_{net} changes resulting from cloud phase treatment are expected and found in the mid-latitudes, as the cloud phase feedback is typically strongest in the extratropics, and as incoming shortwave radiation is larger at lower latitudes.
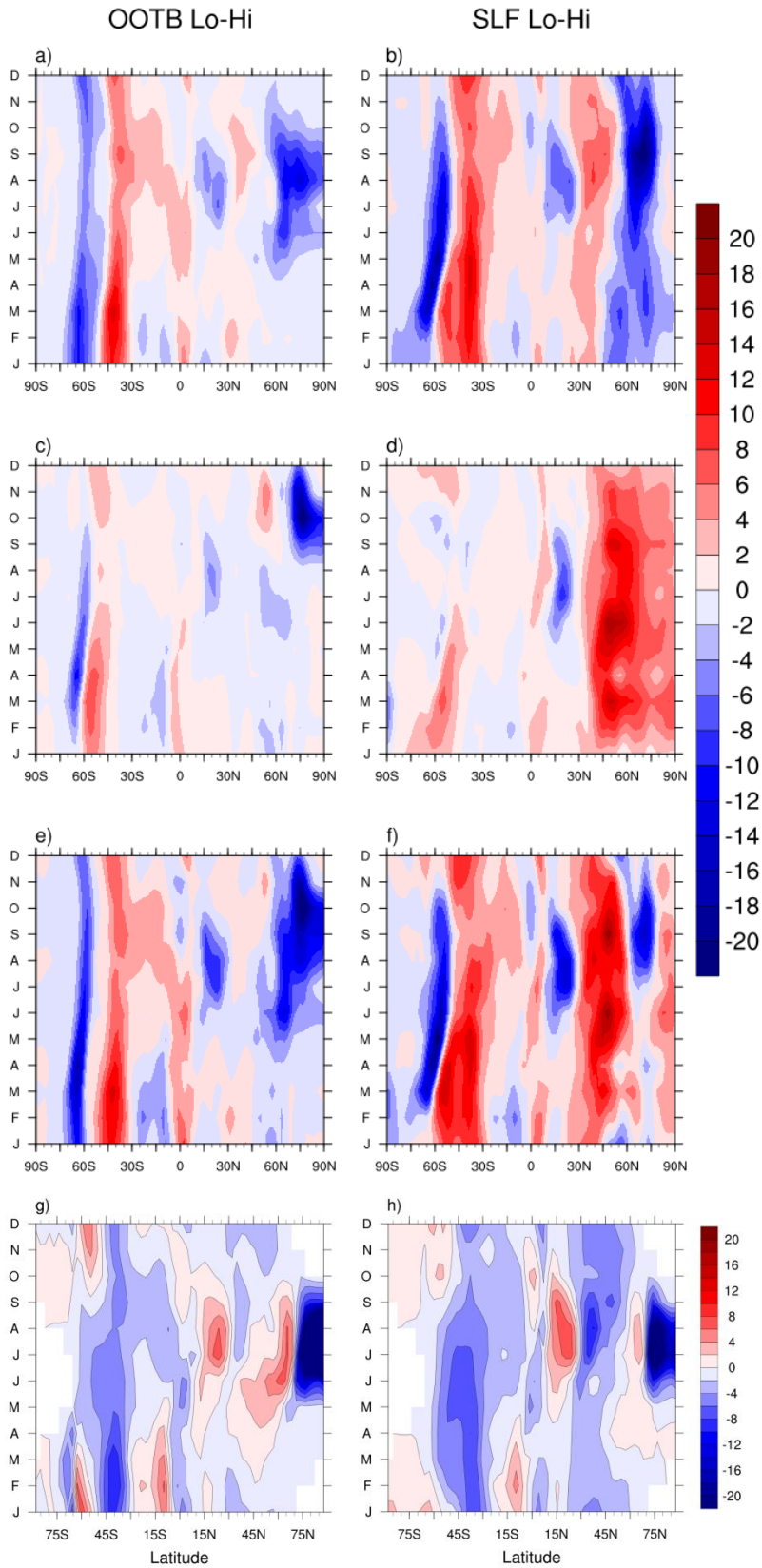
21

Figure 11. Lo-Hi OOTB (left) and SLF (right) SW cloud feedback effect on ΔR_{net} (g, h) (W m^{-2}), and changes in total grid box cloud liquid water path (a, b), cloud ice water path (c, d), and cloud total water path (e, f) (g m^{-2}).
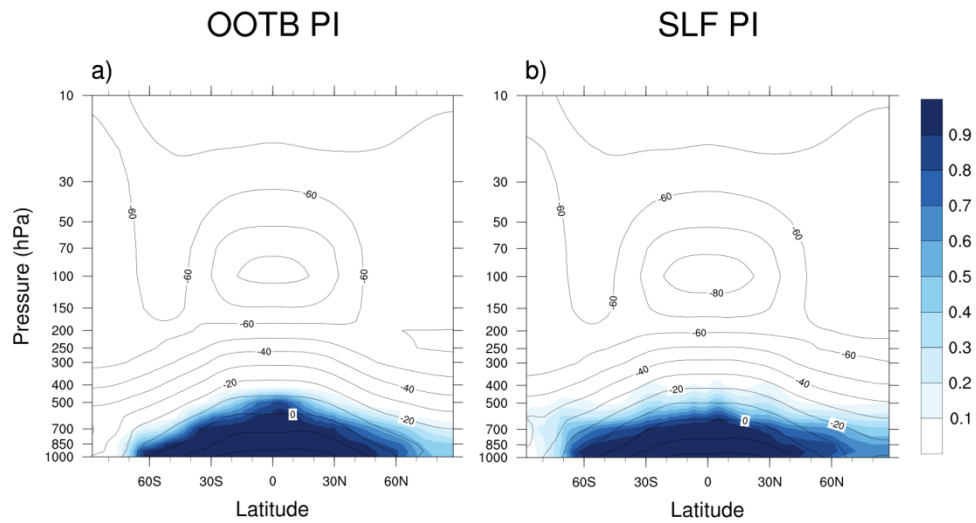
Figure 12. Grid box averaged cloud liquid fraction (colors) and air temperature (°C, contours) for a) OOTB PI and b) SLF PI.
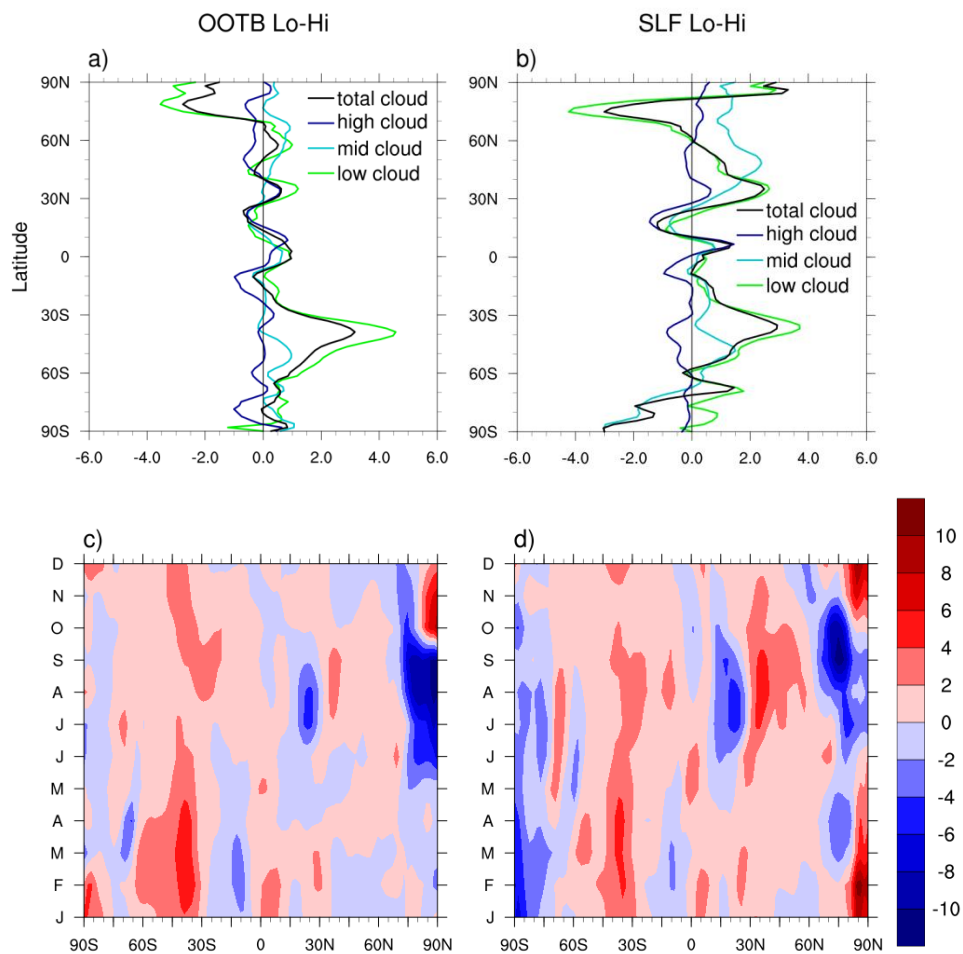

Figure 13. (a, b) Annual changes in zonal mean vertically integrated cloud fraction (%), and (c, d) seasonal changes in zonal mean vertically integrated total cloud fraction (%) for OOTB Lo-Hi (left) and SLF Lo-Hi (right).

23

Higher mid-latitude low and mid-cloud fraction in the SLF Lo-Hi experiment in the NH may also contribute to the enhancement of the SW effect in the mid-latitudes (Fig. 13a, b).

Although the largest reduction in ΔR_{net} from the SW cloud feedback for SLF compared to OOTB occurs in the mid-latitudes, the SW cloud feedback is also the largest contributor other than the water vapor feedback to reduced ΔR_{net} in the tropics in SLF compared to OOTB. This suggests that the weakened and poleward-shifted cloud phase feedback allows cooling to spread more equatorward in SLF, with enhanced tropical cooling then amplified by the water vapor feedback.

Following a similar pattern to that of the albedo and lapse rate feedbacks, the SW cloud feedback in SLF is weaker than in OOTB north of 75°N. The stronger increase in total water path (Fig. 11e, f) and total cloud fraction (Fig. 13c, d) between 75 and 90°N in SLF than in OOTB can likely be attributed to the weaker sea ice growth in SLF, as the stronger sea ice growth in OOTB reduces the open water area and thus reduces the available moisture for clouds to a greater extent. Despite this higher total water path increase in SLF than OOTB between 75 and 90°N, the SLF SW cloud feedback is weaker than that of OOTB Lo-Hi at these latitudes due to the higher initial sea ice extent in SLF, as cloud changes over bright surfaces impact SW radiation to a lesser degree. However, changes in the SW cloud feedback at high latitudes have a much lower impact on the climate response than changes at lower latitudes as much less insolation is received at high latitudes, such that the observed mid-latitude changes in the SW cloud feedback are more important for the climate response than those above 75°N.

While enhanced cooling resulting from a weakened cloud phase feedback in response to reduced obliquity in SLF may contribute to the high latitude cloud ice water path increase, it is also likely that the colder temperatures in SLF PI compared to OOTB PI contribute to the enhanced ice water path in SLF, augmenting the negative SW cloud feedback at high latitudes in this simulation. Nevertheless, differences in cloud phase treatment between SLF and OOTB play an important role in promoting stronger mid- and low latitude cooling in SLF, while the underestimation of SLFs in OOTB produces an overestimated cloud phase feedback in opposition to obliquity-driven cooling. As cloud feedbacks constitute the largest source of uncertainty in model predictions of climate sensitivity (e.g., Soden and Held 2006, Flato et al. 2013), with differences in low cloud amount and in the SW cloud feedback contributing the most to inter-model spread in cloud feedbacks (Soden and Vecchi 2011), these results would benefit

24

from comparison with other models incorporating SLF observational constraints into idealized obliquity-driven simulations.

5. Ice sheet expansion

While paleoclimate records provide evidence for reduced obliquity promoting NH ice sheet growth, previous modeling of reduced obliquity has not shown the widespread increases in perennial snow cover necessary for glacial inception, in part because the modeled summer cloud feedback opposes cooling at high latitudes (Erb et al. 2013). For comparison with these results, we examine the extent to which ice sheet expansion is encouraged by the fast radiative feedbacks in both the OOTB and SLF Lo-Hi experiments. The full ice sheet response is not represented in these experiments due to the lack of dynamic ice sheets and biogeochemistry, and even with these components included, glaciation has historically required the co-occurrence of low obliquity and NH summer aphelion, an orbital configuration producing colder NH summer. The importance of NH summer aphelion in addition to low obliquity for ice sheet growth is further supported by Lee and Poulsen (2008), who find that a modeled shift from the warmer NH summer perihelion to the colder NH summer aphelion produces a NH continental snowfall response 85% as large as the snowfall response to reduced obliquity. Our experiments also do not simulate Pleistocene vegetation or atmospheric greenhouse gas concentrations, the impact of which on the snowfall response to obliquity forcing is unclear (Lee and Poulsen). With these factors precluding an evaluation of the full ice sheet response, our results instead represent the potential for glacial initiation as promoted by fast radiative feedbacks.

The following sections present snowfall accumulation and ablation metrics which generally indicate that enhanced cooling encourages ice sheet expansion to a greater degree in the SLF Lo-Hi experiment than in the OOTB and GFDL Lo-Hi experiments.

a) Melt response

In the GFDL Lo-Hi experiment, Erb et al. (2013) find high latitude surface cooling in all seasons, with summer cooling almost everywhere at high latitudes. Enhanced high latitude cooling extends to lower latitudes in all seasons in SLF Lo-Hi in comparison to OOTB Lo-Hi, with especially large ΔT differences in summer (Fig. 14). The stronger extratropical surface cooling signal in the SLF experiment than in OOTB or GFDL is more consistent with the proxy

record, which provides evidence for North Atlantic cooling by 2 to 4°C during periods of reduced obliquity (Lawrence et al. 2010). One way to gauge the melt response to this cooling signal is via the positive degree-day method, in which melting degree-days are calculated as the product of a) climatological monthly temperature for months with mean temperatures higher than zero degrees Celsius and b) the number of days per month. The Lo-Hi experiment displays a more significant reduction in positive degree-days and thus more potential for reduced summer melting in SLF than in OOTB, with fewer positive degree-days extending into the mid-latitudes and with reductions of more than 50% in the high Arctic (Fig. 15). Up to 50% reductions in positive degree-days in the southern part of Baffin Island are particularly promising for
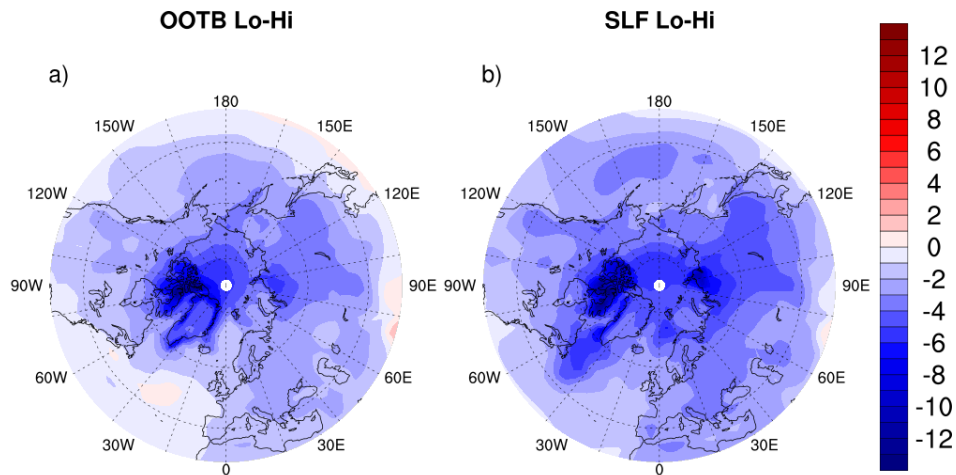

Figure 14. Mean June-July-August ΔT (°C) poleward of 30°N in the a) OOTB and b) SLF Lo-Hi experiments.
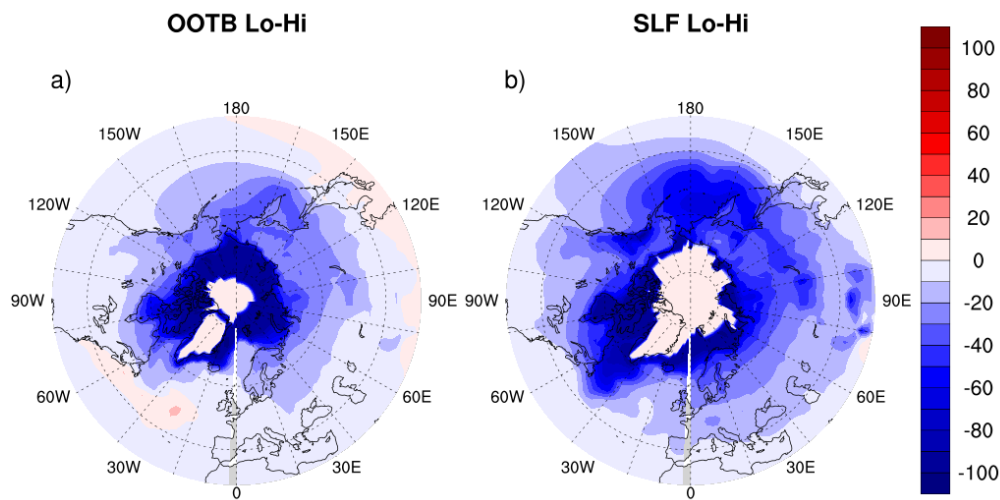

Figure 15. Percent change in annual melting degree-days poleward of 30°N in the a) OOTB and b) SLF Lo-Hi experiments.

glaciation, as this has been deemed a likely location of previous initiation of the Laurentide Ice Sheet based on sediment cores (Clark et al. 1993). Baffin Island is particularly prone to glaciation due to the high elevation of its eastern coast, and as lowering the present-day snowline by only about 300 meters would extend it past a large part of the currently glacier-free area of the island (Williams 1978).

Another method of estimating the potential for melt in each experiment is through a surface energy balance, which is more physically representative of the processes contributing to melt than the positive degree-day method (Bauer et al. 2016). In this approach, the net SW and LW flux at the surface, the sensible (QE) and latent (QL) heat flux at the surface, and the ground heat flux (GE) are summed to find the surface energy available for melting (ME), using the following relation: $SW_{net} + LW_{net} + QE + QL + GE - ME = 0$. Neglecting the negligible ground heat flux term, this surface energy balance is used to calculate the annual melt energy changes shown in Fig. 16. A caveat to using this method is that the existence of an ice sheet would change the surface energy balance in ways that our model does not capture due to its lack of dynamic ice sheets. While there could be changes in sensible and latent heating that increase the energy available for melting if an ice sheet existed, the net solar radiation would decrease due to the enhanced surface albedo of the ice sheet, such that melt energy may be even further reduced in the SLF experiment, in which there appears to be higher potential for ice sheet initiation.

The NH high latitude melt energy reduction estimated in SLF is generally greater than in OOTB, consistent with the larger positive degree-day reduction in SLF, although OOTB exhibits more of a reduction in the upper Arctic Ocean due to the larger sea ice increase here for OOTB.
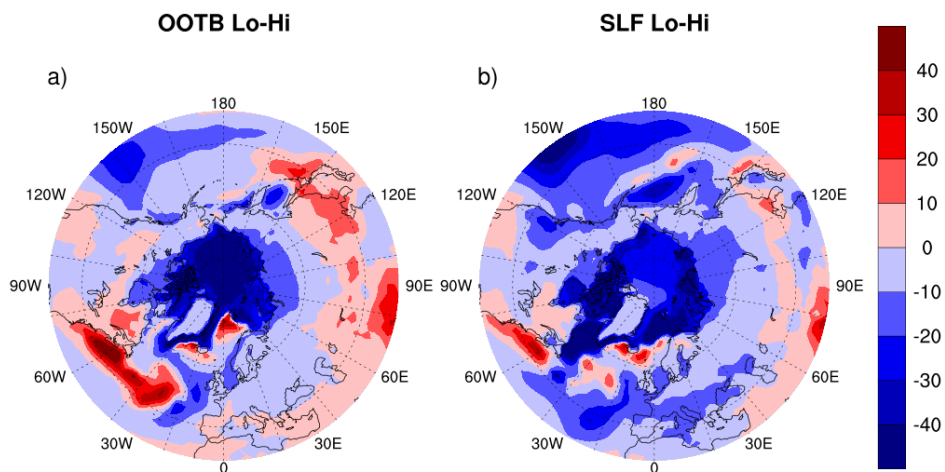

Figure 16. Change in surface melt energy (W m^{-2}) poleward of 30°N in a) OOTB Lo-Hi and b) SLF Lo-Hi.

27

Analysis of each component of the surface energy balance reveals that reduced net SW radiation contributes most to the lower melt energy in SLF Lo-Hi, with the largest SW influences stemming from the albedo and SW cloud feedback at high latitudes.

As in Erb et al. (2013), the effect of the summer cloud feedback on ΔR_{net} for OOTB and SLF Lo-Hi is shown in Fig. 17. Similarly to the GFDL Lo-Hi experiment, OOTB and SLF Lo-Hi both exhibit positive ΔR_{net} due to the summer cloud feedback in some high-latitude regions, reducing cooling in these areas. However, SLF undergoes less warming and more cooling from the summer cloud feedback than OOTB, contributing to reduced melt in SLF. Focusing on the summer cloud feedback effects in the high Canadian Arctic, cooling of the southern part of Baffin Island by the summer cloud feedback in SLF as opposed to warming by this feedback in OOTB seems to promote the reductions in melt energy and positive degree-days modeled in this area, contributing to the enhanced ice sheet initiation potential observed in SLF.
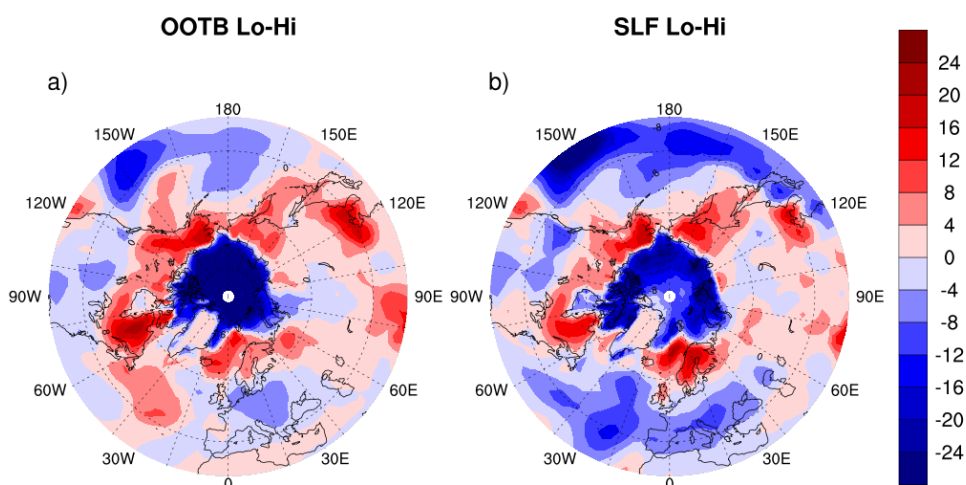

Figure 17. Mean June-July-August ΔR_{net} from the cloud feedback (W m^{-2}) for a) OOTB Lo-Hi and b) SLF Lo-Hi.

b) Snowfall response

The snowfall response to reduced obliquity accounts for a smaller portion of the differences in ice sheet initiation potential between OOTB and SLF than the melt response. Consistent with Lee and Poulsen (2008), the continental snowfall response to reduced obliquity is strongest in the summer and is mainly due to changes in non-convective stable snowfall, which are tied to colder high latitude temperatures and enhanced moisture transport in reduced

obliquity simulations. NH Lo-Hi changes in mean continental summer stable snowfall are .0010 mm/hr (SLF) and .00040 mm/hr (OOTB) while NH mean continental summer stable snowfall values for PI are .0016 mm/hr (SLF) and .00066 mm/hr (OOTB), constituting 67% (SLF) and 60% (OOTB) changes for the Lo-Hi experiments compared to the PI simulations. Figure 18 illustrates much larger increases in continental summer stable snowfall in high latitude NH regions in SLF than OOTB Lo-Hi, although SLF PI exhibits slightly higher snowfall rates to start than OOTB PI.

As explained by Lee and Poulsen (2008), the enhanced summer meridional insolation gradient in reduced obliquity simulations (Fig. 4a) increases the summer equator-to-pole temperature gradient and may contribute to summer poleward vapor transport by transient eddies, providing moisture for enhanced snowfall at high latitudes. The other main cause of increased NH snowfall in response to reduced obliquity is the local reduction of air temperatures at high latitudes as a result of reduced insolation amplified by climate feedbacks. Reduced temperatures promote enhanced snowfall by transforming rainfall to snowfall and by increasing
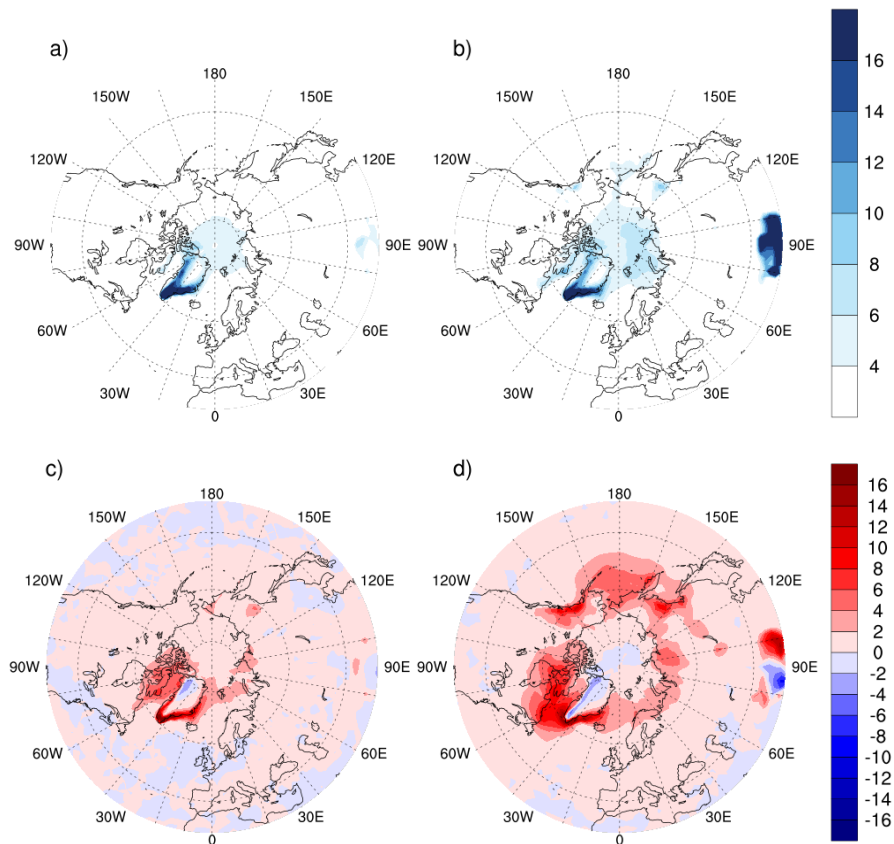

Figure 18. Mean June-July-August large-scale stable snowfall rate (10^{-9} m/s; water equivalent) above 30 °N in the NH for a) OOTB and b) SLF PI, and change in this summer stable snowfall rate for c) OOTB and d) SLF Lo-Hi.

29

atmospheric saturation as a result of reduced saturation vapor pressure following the Clausius-Clapeyron relation (Lee and Poulsen 2008). While the SLF and OOTB experiments have identical summer meridional insolation gradients and similar summer meridional temperature gradients (Fig. 4), such that large moisture transport differences would not be expected, the stronger local reduction of summer air temperatures in SLF (Fig. 14) likely contributes to the enhanced summer snowfall change in SLF relative to OOTB.

Both reduced melt potential and enhanced summer stable snowfall in SLF Lo-Hi contribute to the observed June-July-August change in snow depth over land given in Fig. 19, with up to a meter of increased water equivalent snow depth over the southern part of Baffin Island in SLF Lo-Hi compared to OOTB Lo-Hi. As increased perennial snow cover would be required for ice sheet initiation, and as Baffin Island is a historically likely location for this initiation, the stronger persistence of June-July-August snow in SLF suggests a greater potential for glacial inception in this experiment than is found in OOTB or in GFDL. It is also likely that these experiments underestimate the snow depth response due to the low spatial resolution of the models, which do not capture the elevated topography in northeastern Canada and Scandinavia, such that increases in snow depth may be even larger than the modeled results (Jochum et al. 2012).
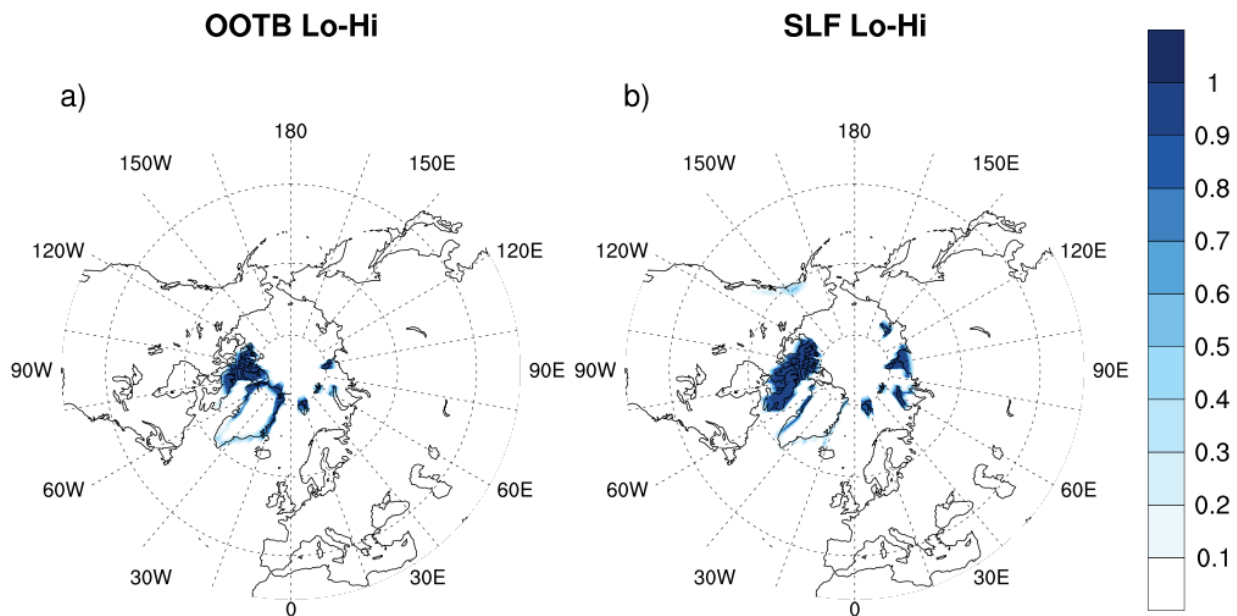

Figure 19. Mean June-July-August change in snow depth over land (m; water equivalent) poleward of 30°N in the a) OOTB Lo-Hi and b) SLF Lo-Hi experiments.

6. Ongoing analysis

a) Simulation Retuning

As modeled feedbacks and temperature reductions in response to obliquity forcing are partly dependent on the colder initial temperatures and higher initial sea ice fraction in SLF PI compared to OOTB PI, ongoing simulation retuning of the SLF experiments is aimed at bringing the simulated temperature in the SLF PI experiment closer to that of OOTB PI. As a result, modeled climate changes will be attributable exclusively to the cloud phase modifications in the SLF model. While current results already indicate the importance of model differences in cloud phase for the SW cloud feedback and, as a result, the water vapor feedback, retuning will allow for a more conclusive evaluation of the effect of cloud phase treatment on the climate response to reduced obliquity.

b) Cloud radiative feedback partitioning

In order to further explore the contributions of cloud amount, altitude, and optical depth to the total cloud feedback, the cloud feedback will be partitioned following Zelinka et al. (2012b) when the retuned SLF Lo-Hi experiment output is available. In this approach, histograms of cloud fraction changes as a function of cloud top pressure (CTP) and optical depth (τ) will be generated by incorporating the International Satellite Cloud Climatology Project satellite simulator (ISCCP; Klein and Jakob 1999; Webb et al. 2001) into the OOTB and SLF CESM simulations, while cloud radiative kernels have been obtained from Zelinka et al. (2012a) to quantify the impact of cloud fraction changes in each histogram bin on the TOA radiative budget. Multiplying the ISCCP-simulated cloud changes and the cloud radiative kernels will then provide an estimate of the effect of cloud amount, altitude, and optical depth feedbacks on TOA radiation. As cloud phase is an important factor in determining cloud optical depth, we would expect the largest differences in the SW cloud feedback between OOTB and SLF Lo-Hi to be attributed to differences in optical depth, with optically thicker clouds in SLF resulting from the weakened liquid-to-ice cloud phase transition in this experiment.

7. Conclusions

This study compared the results of reduced obliquity simulations using an out-of-the-box CESM-CAM5.1 model and a CESM-CAM5.1 model with the observational constraints on cloud

phase partitioning developed by Tan et al. (2016), additionally relating the modeled climate response to that observed in Erb et al. (2013) using the GFDL-CM2.1 model. The purpose of this comparison was to determine the impact of a more realistic representation of cloud supercooled liquid fractions on the climate response to reduced obliquity. As GFDL-CM2.1 is one of many GCMs that underestimate supercooled liquid, producing an overestimated positive effect on net TOA radiation resulting from the cloud phase feedback, we expected a more realistic cloud phase partitioning scheme to amplify cooling in the SLF Lo-Hi experiment.

The SLF Lo-Hi experiment exhibits enhanced negative global mean ΔR_{net} and enhanced cooling when compared with GFDL and OOTB Lo-Hi, with the extension of cooling to the tropics in SLF drawing closer to the paleoclimate record of the climate response to reduced obliquity than the tropical warming modeled in OOTB and GFDL. The largest contributions to the stronger negative ΔR_{net} in SLF Lo-Hi arise from the SW cloud and water vapor feedbacks. A weakened cloud phase feedback contributes to the stronger negative SW cloud feedback particularly in the mid-latitudes, but also contributes to enhanced tropical cooling in SLF, which is amplified by the water vapor feedback.

As we also found differences in air temperature and sea ice in the OOTB and SLF PI simulations, with colder temperatures and greater sea ice extent in SLF PI, the climate response in the Lo-Hi simulations cannot be attributed solely to cloud phase changes, and the colder initial SLF climate likely contributes to extended cooling in SLF Lo-Hi. Nevertheless, liquid water path enhancement as a result of weakened cloud phase transitions in SLF Lo-Hi plays an important role in promoting cooling in this experiment and in allowing for the extension of $-\Delta T$ to lower latitudes.

As a result of the stronger cooling signal in SLF Lo-Hi, reduced melting and enhanced summer snowfall at high latitudes in this experiment encourage stronger persistence of perennial snow cover than modeled in OOTB Lo-Hi or GFDL Lo-Hi. The result is a greater potential for ice sheet initiation in SLF Lo-Hi, although our ability to assess ice sheet growth is limited by the lack of dynamic ice sheets in these simulations. As mentioned by Erb et al. (2013), inclusion of dynamic ice sheets may also impact the modeled climate feedbacks, which would likely change over time following the evolution of ice sheets.

While ongoing retuning and cloud feedback partitioning should clarify the extent to which changes in cloud phase treatment produce differences in the climate response of the SLF

and OOTB experiments, this study complements existing literature on the importance of cloud phase for the modeled climate sensitivity to modern-day forcing from CO_2-doubling, as we find that cloud phase representation can also significantly alter the modeled climate response to obliquity forcing. By allowing for an amplified climate and ice sheet response to reduced obliquity, observational constraints on cloud phase bring us closer to simulating the paleoclimate record and to resolving the 41-kyr paradox.

References

E. Bauer, and A. Ganopolski, Comparison of surface mass balance of ice sheets simulated by positive-degree-day method and energy balance approach, Clim. Past Discuss., in review (2016).

A. Berger, and M. F. Loutre, Insolation values for the climate of the last 10 million years. Quat. Sci. Rev. 10, 297–317 (1991).

S. Bony, et al., How well do we understand and evaluate climate change feedback processes? J. Climate 19, 3445–3482 (2006).

G. Cesana, D. E. Waliser, X. Jiang, J. L. Li, Multimodel evaluation of cloud phase transition using satellite and reanalysis data. J. Geophys. Res. 120, 7871–7892 (2015).

P. U. Clark, et al., Initiation and development of the Laurentide and Cordilleran ice sheets following the last interglaciation. Quat. Sci. Rev. 12, 79–114 (1993).

E. Cortijo, S. Lehman, L. Keigwin, M. Chapman, D. Paillard, and L. Labeyrie, Changes in meridional temperature and salinity gradients in the North Atlantic Ocean (30–70 N) during the last interglacial period. Paleoceanography 14, 23–33 (1999).

T. L. Delworth et al., GFDL's CM2 global coupled climate models. Part I: Formulation and simulation characteristics. J. Climate 19, 643–674 (2006).

L. J. Donner et al., The Dynamical Core, Physical Parameterizations, and Basic Simulation Characteristics of the Atmospheric Component AM3 of the GFDL Global Coupled Model CM3. J. Climate 24, 3484–3519 (2011).

M. P. Erb, A.J. Broccoli, and A.C. Clement, The Contribution of Radiative Feedbacks to Orbitally Driven Climate Change. J. Climate 26, 5897–5914 (2013).

G. Flato, J. Marotzke, B. Abiodun, P. Braconnot, S.C. Chou, W. Collins, P. Cox, F. Driouech, S. Emori, V. Eyring, C. Forest, P. Gleckler, E. Guilyardi, C. Jakob, V. Kattsov, C. Reason and M. Rummukainen, Evaluation of Climate Models (2013). In: Climate Change 2013: The Physical Science Basis. Contribution of Working Group I to the Fifth Assessment Report of the Intergovernmental Panel on Climate Change [Stocker, T.F., D. Qin, G.-K. Plattner, M. Tignor, S.K. Allen, J. Boschung, A. Nauels, Y. Xia, V. Bex and P.M. Midgley (eds.)]. Cambridge University Press, Cambridge, United Kingdom and New York, NY, USA.

GFDL Global Atmospheric Model Development Team, The new GFDL global atmosphere and land model AM2/LM2: Evaluation with prescribed SST simulations. J. Climate 17, 4641–4673 (2004).

J. D. Hays, J. Imbrie, and N. J. Shackleton, Variations in the earth's orbit: Pacemaker of the ice ages. Science 194, 1121–1132 (1976).

D. A. Hodell, The smoking gun of the ice ages. Science 354, 1235-1236 (2016).

E. C. Hunke, and W. H. Lipscomb, CICE: The Los Alamos sea ice model, documentation and software, version 4.0. Los Alamos National Laboratory Tech. Rep. LACC-06-012, 76 pp. (2008).

J. W. Hurrell, M.M. Holland, P.R. Gent, S.S. Ghan, J.E. Kay, P.J. Kushner, J.F. Lamarque, W.G. Large, D.D. Lawrence, K.K. Lindsay, W.H. Lipscomb, M.C. Long, N.N. Mahowald, D.R. Marsh, R.B. Neale, P.P. Rasch, S.S. Vavrus, M.M. Vertenstein, D.D. Bader, W.D. Collins, J.J. Hack, J.J. Kiehl, and S.S. Marshall, The Community Earth System Model: A Framework for Collaborative Research. Bull. Amer. Meteor. Soc. 94, 1339–1360 (2013).

J. Imbrie et al., On the structure and origin of major glaciations cycles 2. The 100,000-year cycle. Paleoceanography 8, 699–735 (1993).

M. Jochum, A. Jahn, S. Peacock, D. A. Bailey, J. T. Fasullo, J. Kay, S. Levis, and B. Otto-Bliesner, True to Milankovitch: Glacial inception in the new Community Climate System Model. J. Climate 25, 2226–2239 (2012).

S. A. Klein, and C. Jakob, Validation and sensitivities of frontal clouds simulated by the ECMWF model. Mon. Wea. Rev. 127, 2514–2531 (1999).

M. Komurcu, T. Storelvmo, I. Tan, U. Lohmann, Y. Yun, J. E. Penner, Y. Wang, X. Liu, T. Takemura, Intercomparison of the cloud water phase among global climate models. J. Geophys. Res. 119, 3372–3400 (2014).

D. M. Lawrence, K. W. Oleson, M. G. Flanner, P. E. Thornton, S. C. Swenson, P. J. Lawrence, X. Zeng, Z.-L. Yang, S. Levis, K. Sakaguchi, G. B. Bonan, and A. G. Slater, Parameterization improvements and functional and structural advances in version 4 of the Community Land Model. J. Adv. Model. Earth Syst. 3, M03001 (2011).

K. T. Lawrence, S. Sosdian, H. E. White, and Y. Rosenthal, North Atlantic climate evolution through the Plio-Pleistocene climate transitions. Earth Planet. Sci. Lett. 300, 329–342 (2010).

S.-Y. Lee, and C. J. Poulsen, Tropical Pacific climate response to obliquity forcing in the Pleistocene. Paleoceanography, 20, PA4010 (2005).

S.-Y. Lee, and C. J. Poulsen, Amplification of obliquity forcing through mean annual and seasonal atmospheric feedbacks. Climate Past 4, 515–534 (2008).

L.E. Lisiecki, and M. E. Raymo, A Pliocene-Pleistocene stack of 57 globally distributed benthic delta O-18 records. Paleoceanography 20, PA1003 (2005).

D.F. Mantsis, A. C. Clement, A. J. Broccoli, and M. P. Erb, Climate feedbacks in response to changes in obliquity. J. Climate 24, 2830–2845 (2011).

M. Maslin, In retrospect: Forty years of linking orbits to ice ages. Nature 540, 208-210 (2016).

M. Milankovitch, Kanon der Erdbestrahlung und seine Anwendung auf das Eiszeitenproblem (Canon of Insolation and the Ice-Age Problem). Royal Serbian Academy, Special Publication, 133, 633 pp. (1941).

B. J. Murray, D. O'Sullivan, J. D. Atkinson, M. E. Webb, Ice nucleation by particles immersed in supercooled cloud droplets. Chem. Soc. Rev. 41, 6519–6554 (2012).

R. B. Neale et al., Description of the NCAR Community Atmosphere Model (CAM5.0). NCAR Tech. Note NCAR/TN-486+ STR (2012).

K. W. Oleson et al., Technical description of version 4.0 of the Community Land Model (CLM). NCAR Tech. Note NCAR/TN-478+STR, 257 pp. (2010).

J. P. Phillips, and I. M. Held, The response to orbital perturbations in an atmospheric model coupled to a slab ocean. J. Climate 7, 767–782 (1994).

H. R. Pruppacher, J. D. Klett, Microphysics of Clouds and Precipitation 1980 (Reidel, Dordrecht, Netherlands, 1978).

M. E. Raymo, and K. Nisancioglu, The 41 kyr world: Milankovitch's other unsolved mystery. Paleoceanography 18, 1011 (2003).

T. Reichler, and J.Kim, How well do coupled models simulate today's climate? Bull. Amer. Meteor. Soc. 89, 303–311 (2008).

L. D. Rotstayn, B. F. Ryan, and J. Katzfey, A scheme for calculation of the liquid fraction in mixed-phase clouds in large-scale models. Mon. Wea. Rev. 128, 1070–1088 (2000).

K. M. Shell, J. T. Kiehl, and C. A. Shields, Using the radiative kernel technique to calculate climate feedbacks in NCAR's Community Atmospheric Model. J. Clim. 21, 2269-2282 (2008).

R. D. Smith, R. D. et al., The Parallel Ocean Program (POP) reference manual: Ocean component of the Community Climate System Model (CCSM) and Community Earth System Model (CESM). Los Alamos National Laboratory Tech. Rep. LAUR-10-01853,141 pp. (2010).

B. J. Soden, and I. M. Held, An assessment of climate feedbacks in coupled ocean–atmosphere models. J. Climate 19, 3354–3360 (2006).

B. J. Soden, I. M. Held, R. Colman, K. M. Shell, J. T. Kiehl, and C. A. Shields, Quantifying climate feedbacks using radiative kernels. J. Climate 21, 3504–3520 (2008).

B. J. Soden, and G. A. Vecchi, The vertical distribution of cloud feedback in coupled ocean-atmosphere models. Geophys. Res. Lett. 38, L12704 (2011).

T. Storelvmo, I. Tan, A. V. Korolev, Cloud phase changes induced by CO_2 warming—A powerful yet poorly constrained cloud-climate feedback. Curr. Clim. Change Rep. 1, 1-9 (2015).

I. Tan, T. Storelvmo, M. D. Zelinka, Observational constraints on mixed-phase clouds imply higher climate sensitivity. Science 352, 224-227 (2016).

F. Vimeux, V. Masson, G. Delaygue, J. Jouzel, J. R. Petit, and M. Stievenard, A 420,000 year deuterium excess record from East Antarctica: Information on past changes in the origin of precipitation at Vostok, J. Geophys. Res.-Atmos. 106, 31 863–31 873 (2001).

M. Webb, C. Senior, S. Bony, and J. J. Morcrette, Combining ERBE and ISCCP data to assess clouds in the Hadley Centre, ECMWF and LMD atmospheric climate models. Climate Dyn. 17, 905–922 (2001).

L. D. Williams, The Little Ice Age glaciation level on Baffin Island, Arctic Canada Palaeogeogr. Palaeoclimatol. Palaeoecol. 25, 199–207 (1978).

M. D. Zelinka, S. A. Klein, D. L. Hartmann, Computing and partitioning cloud feedbacks using cloud property histograms. Part I: Cloud Radiative Kernels. J. Clim. 25, 3715-3735 (2012).

M. D. Zelinka, S. A. Klein, D. L. Hartmann, Computing and partitioning cloud feedbacks using cloud property histograms. Part II: Attribution to changes in cloud amount, altitude and optical depth. J. Clim. 25, 3736–3754 (2012).

Appendix A

Table A1. Global annual-mean effect of climate feedbacks on ΔR_{net} (W m^{-2}).

Feedback	GFDL Lo-Hi*	OOTB Lo-Hi	SLF Lo-Hi
Surface albedo	-0.27 (13%)	-0.64 (23%)	-0.84 (19%)
Water vapor	-0.20 (10%)	-0.09 (3%)	-1.02 (23%)
Lapse rate	-0.90 (44%)	-1.03 (37%)	-0.85 (19%)
Cloud	-0.67 (33%)	-1.04 (37%)	-1.77 (39%)
SW Cloud	**	-1.26	-2.08
LW Cloud	**	0.22	0.30
Total	-2.03	-2.80	-4.49

*Values obtained from Erb et al. (2013).
**Not given.

Table A2. Regional annual-mean effect of climate feedbacks on ΔR_{net} (W m^{-2}).

Feedback	Latitude	OOTB Lo-Hi	SLF Lo-Hi
Surface albedo	+/- 30°-60°	-0.18	-0.96
	+/- 60°-90°	-4.77	-4.02
	Polar (70°-90°)	-9.79	-7.54
	Tropics (-30° to 30°)	0.03	0.01
	Extratropics (+/-30°-90°)	-1.34	-1.73
Water vapor	+/- 30°-60°	-0.21	-0.86
	+/- 60°-90°	-0.14	-0.45
	Polar (70°-90°)	-0.14	-0.35
	Tropics (-30° to 30°)	0.01	-1.27
	Extratropics (+/-30°-90°)	-0.19	-0.76
Lapse rate	+/- 30°-60°	-0.91	-1.45
	+/- 60°-90°	-5.55	-4.88
	Polar (70°-90°)	-12.02	-10.65
	Tropics (-30° to 30°)	-0.02	0.56
	Extratropics (+/-30°-90°)	-2.08	-2.31
Cloud	+/- 30°-60°	-1.57	-2.85
	+/- 60°-90°	-1.42	-0.24
	Polar (70°-90°)	-6.82	-4.18
	Tropics (-30° to 30°)	-0.57	-1.37
	Extratropics (+/-30°-90°)	-1.53	-2.19
SW Cloud	+/- 30°-60°	-1.91	-3.64
	+/- 60°-90°	-2.55	-1.59
	Polar (70°-90°)	-9.08	-6.54
	Tropics (-30° to 30°)	-0.49	-1.07
	Extratropics (+/-30°-90°)	-2.07	-3.12
LW Cloud	+/- 30°-60°	0.34	0.79
	+/- 60°-90°	1.14	1.34
	Polar (70°-90°)	2.27	2.36
	Tropics (-30° to 30°)	-0.08	-0.30
	Extratropics (+/-30°-90°)	0.54	0.93